

# Modeling Chemical Exfoliation of Non-van der Waals Chromium Sulfides by Machine Learning Interatomic Potentials and Monte Carlo Simulations

Published as part of *The Journal of Physical Chemistry C virtual special issue "Machine Learning in Physical Chemistry Volume 2"*.

Akram Ibrahim, Daniel Wines, and Can Ataca\*

Cite This: <https://doi.org/10.1021/acs.jpcc.3c06168>

Read Online

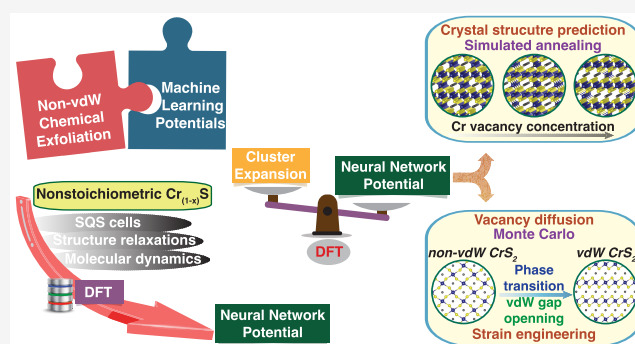
ACCESS |

Metrics & More

Article Recommendations

Supporting Information

**ABSTRACT:** The chemical exfoliation of non-van der Waals (vdW) materials to ultrathin nanosheets remains a formidable challenge. This difficulty arises from the strong preference of these materials to engage in three-dimensional chemical bonding, resulting in uncontrolled atomic migration into the vdW gaps during cation deintercalation from the bulk structure, ultimately leading to unpredictable structural disorder. Computational models capable of comprehending the widespread nonstoichiometric local environments resulting from disordered atomic migrations during the exfoliation of non-vdW materials are crucial for understanding the underlying mechanisms. Here, we propose a generic framework using neural network potentials (NNPs) to accurately model nonstoichiometric systems over a broad range of vacancy concentrations. We apply our framework to investigate the crystal structures and phase transformations occurring during the exfoliation of non-vdW nonstoichiometric  $\text{Cr}_{(1-x)}\text{S}$  systems, a compelling material category with substantial potential for two-dimensional (2D) magnetic applications. The efficacy of the NNP outperforms conventional cluster expansion, exhibiting superior accuracy and transferability to unexplored crystal structures and compositions. By employing the NNP in simulated annealing optimizations, we predict low-energy  $\text{Cr}_{(1-x)}\text{S}$  structures anticipated to result from experimental synthesis. A notable structural transition is discerned at the  $\text{Cr}_{0.5}\text{S}$  composition, with half of the Cr atoms preferentially migrating to vdW gaps. This aligns with experimental observations in the chemical exfoliation of 2D  $\text{CrS}_2$  and emphasizes the vital role of excess Cr atoms beyond the  $\text{Cr}/\text{S} = 1/2$  composition ratio in stabilizing vdW gaps. Additionally, we utilize the NNP in a large-scale vacancy diffusion Monte Carlo simulation to illustrate the impact of lateral compressive strains in catalyzing the formation of vdW gaps within non-vdW  $\text{CrS}_2$  slabs through Poisson's axial expansion. This provides a direct pathway for more facile exfoliation of ultrathin nanosheets from non-vdW materials through strain engineering. The implemented methodology, leveraging machine learning potentials, is imperative to bridge the quantum-level accuracy to large scales necessary for modeling the intricate mechanisms underlying the chemical exfoliation of non-vdW materials.



## 1. INTRODUCTION

Recent years have witnessed significant progress in the synthesis of two-dimensional (2D) nanosheets derived from materials that lack a layered van der Waals (vdW) parent structure, broadening the scope of exfoliation research to encompass a wide variety of previously unexplored 2D non-vdW materials.<sup>1,2</sup> Among the family of non-vdW materials, Cr-based compounds, particularly magnetic non-vdW Cr–S materials, have garnered substantial attention within the field of 2D magnetic materials with a myriad of potential applications in electronic and spintronic devices,<sup>1,3,4</sup> especially following the discovery of 2D magnets like  $\text{CrI}_3$  and  $\text{CrGeTe}_3$ .<sup>5,6</sup> The Cr–S system comprises a minimum of six

distinct known phases, namely,  $\text{CrS}$ ,  $\text{Cr}_7\text{S}_8$ ,  $\text{Cr}_5\text{S}_6$ ,  $\text{Cr}_3\text{S}_4$ ,  $\text{Cr}_2\text{S}_3$ , and  $\text{Cr}_5\text{S}_8$ ,<sup>7</sup> all exhibiting a hexagonal NiAs-type structure, with vacancies in the Cr sublattice responsible for the formation of nonstoichiometric phases.  $\text{Cr}_2\text{S}_3$  is the most stable phase, attributed to Cr's preference for the 3+ oxidation state.

**Received:** September 13, 2023

**Revised:** December 27, 2023

**Accepted:** December 28, 2023

Recently, nanothick 2D Cr–S slabs have been successfully fabricated. For example, Cr<sub>2</sub>S<sub>3</sub> flakes with the thickness ranging from tens of nanometers down to a single unit cell (~1.8 nm) were synthesized using chemical vapor deposition (CVD).<sup>8,9</sup> The resulting 2D Cr<sub>2</sub>S<sub>3</sub> material is a semiconductor with ferrimagnetic ordering and a Néel temperature of around 120 K. Additionally, few-nanometer-thick 2D flakes of 1T-CrS<sub>2</sub> were synthesized using CVD, exhibiting metallic behavior and room-temperature ferromagnetism.<sup>10</sup> Moreover, a semiconducting H<sub>x</sub>CrS<sub>2</sub> crystalline/amorphous layered material, exhibiting antiferromagnetic ordering and a Néel temperature of 5 K, was synthesized with a thickness of 2–3 nm using chemical exfoliation.<sup>7</sup>

The strong interlayer binding inherent in bulk non-vdW-layered materials constitutes a formidable barrier to conventional mechanical exfoliation methods. Consequently, alternative approaches such as chemical exfoliation or direct liquid-phase exfoliation (LPE) are commonly employed for the top-down synthesis of non-vdW materials. Chemical exfoliation is especially pertinent for crystal structures that do not naturally exist in pristine bulk form, whether as vdW or non-vdW structures.<sup>11</sup> This is particularly evident in the case of Cr dichalcogenides, i.e., CrX<sub>2</sub> (where X = S, Se, and Te), which do not naturally exist in a bulk transition-metal dichalcogenide (TMD)-layered or pyrite form.<sup>7</sup> Nevertheless, these structures can be identified in other ternary compounds, such as ACrX<sub>2</sub> (where A = Li, Na, and K).<sup>7,12,13</sup> These ternary compounds can serve as base structures for synthesizing Cr 2D TMDs through chemical exfoliation. The initial step in chemical exfoliation involves the removal of extraneous cations present in the base bulk structure through either cation exchange or oxidative removal. For instance, proton exchange with Na in NaCrS<sub>2</sub> using HCl/ethanol solution<sup>7</sup> and K deintercalation from both KCrSe<sub>2</sub><sup>13,14</sup> and KCrTe<sub>2</sub><sup>15</sup> through I<sub>2</sub> oxidation have been employed during the chemical exfoliation of CrS<sub>2</sub>, CrSe<sub>2</sub>, and CrTe<sub>2</sub> structures, respectively. The second step of chemical exfoliation involves LPE to induce fragmentation and delamination of the atomic layers from the formed bulk structures. However, owing to the strong tendency of non-vdW materials to form three-dimensional (3D) chemical bonds, they undergo uncontrolled cation migration from the layers (Cr atoms within CrS<sub>2</sub> layers in this context) to the vdW gaps during the initial deintercalation process, thereby retaining their non-vdW characteristics.<sup>7,11,13,16</sup> As a consequence, the exfoliated 2D sheets typically exhibit thicknesses on the order of several nanometers, thereby impeding the realization of the distinct properties observable in monolayer-thin sheets, characterized by enhanced quantum confinement and reduced interlayer interactions. As a result, there is growing interest in developing computational methods to achieve a deeper understanding and, consequently, greater control over the chemical exfoliation of ultrathin nanosheets from these non-vdW crystals.

Nonstoichiometric local atomic environments, characterized by varying elevated vacancy concentrations, are commonly observed in chemical exfoliation processes.<sup>7,11</sup> The ubiquity of these nonstoichiometric environments can be attributed to the disordered atomic migration that occurs following the deintercalation process associated with the chemical exfoliation of non-vdW materials.<sup>7</sup> This phenomenon leads to distinct compositional variations that are evident both temporally and spatially. Consequently, to gain insights into the intricate mechanisms underlying the chemical exfoliation of non-vdW

materials, it is imperative to develop accurate computational models capable of comprehending nonstoichiometric environments across a wide range of vacancy concentrations. Modeling nonstoichiometric systems exclusively through density functional theory (DFT) proves infeasible due to the extensive spectrum of conceivable compositions and atomic configurations, which escalates exponentially with the number of atoms in the unit cell.<sup>17</sup> To mitigate this challenge, researchers commonly employ special quasi-random structure (SQS) cells<sup>18,19</sup> as representative unit cells that effectively capture the statistical features of atomic disorder, enabling DFT predictions for compositions attainable within compact unit cells. To extrapolate to other compositions or facilitate large-scale simulations, the common practice is to employ a surrogate model like cluster expansion (CE).<sup>20–22</sup> While the on-lattice CE is well-suited for fixed-lattice alloy systems, nonstoichiometric systems frequently manifest significant deviations from the parent lattice and exhibit notable sensitivity of atomic arrangements to mechanical strains.<sup>23–25</sup> Therefore, a more dependable approach entails adopting an off-lattice model that incorporates both configurational and geometrical features of nonstoichiometric systems. Additionally, CE's transferability to unobserved on-lattice configurations and compositions remains a subject warranting further investigation.<sup>26</sup>

Machine learning potentials (MLPs) have recently emerged as highly promising tools in computational materials science due to their near-DFT accuracy, nearly linear scaling with system size, and exceptional transferability to diverse chemical environments. Prominent examples of MLPs include neural network potentials (NNPs),<sup>27–30</sup> Gaussian approximation potentials,<sup>31,32</sup> moment tensor potentials,<sup>33</sup> spectral neighbor analysis potentials,<sup>34</sup> atomic CE potentials,<sup>35,36</sup> and graph NNPs.<sup>37–39</sup> The high flexibility of MLPs allows for broad applicability across different types of matter, encompassing bulk<sup>40–42</sup> and 2D crystals,<sup>43</sup> amorphous materials,<sup>44,45</sup> liquids,<sup>46–48</sup> interfaces,<sup>49,50</sup> and clusters.<sup>51,52</sup> In the domain of disordered systems, MLPs were employed to investigate binary alloys spanning a wide range of compositions,<sup>53–57</sup> high-entropy alloys,<sup>58–60</sup> and grain boundaries.<sup>61–64</sup> However, a conspicuous gap exists in the literature concerning the application of MLPs to nonstoichiometric systems characterized by varying elevated vacancy concentrations. Herein, we address this gap by examining the efficacy of NNPs for modeling nonstoichiometric chromium sulfides, a material that has not been explored in the existing literature using either machine learning or conventional potentials.

In this study, we present a general workflow for modeling nonstoichiometric systems using NNPs (Methods). The NNP's performance is demonstrated to surpass that of CE, showcasing near-DFT accuracy and remarkable transferability to unobserved structures exhibiting diverse compositions (Results, 3.1). By incorporating the NNP into simulated annealing (SA) optimizations (Results, 3.2), we gain insights into the low-energy ground-state and metastable Cr–S structures that are anticipated to result from experimental synthesis. The outcomes highlight the crucial role played by the surplus Cr atoms beyond the Cr/S = 1/2 ratio in stabilizing the vdW gaps. Moreover, a notable structural transition is observed for the CrS<sub>2</sub> phase, characterized by a preferential migration of half of the Cr atoms to the vdW gaps. This finding aligns with experimental observations, illuminating the non-vdW nature of 2D CrS<sub>2</sub>. Moreover, we leverage the NNP in a

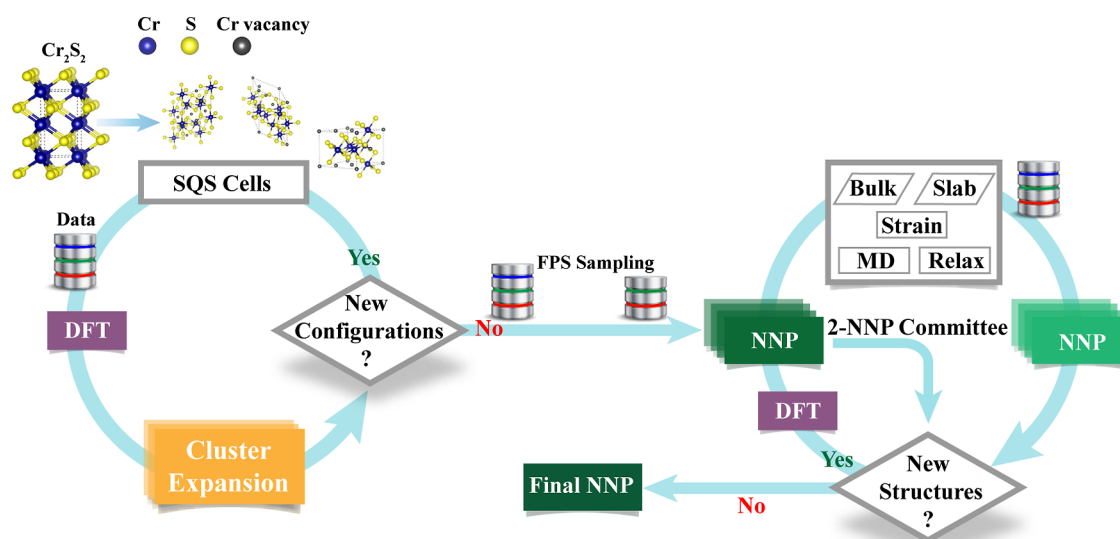


**Figure 1.** NNP generation workflow. The first part (loop on the left) involves the utilization of the CE Hamiltonian to iteratively sample small SQS cells (<20 atoms) toward ground states at 22 distinct compositions. The NNP is first trained on snapshots, sampled using a FPS algorithm, from the DFT relaxations performed for CE-sampled SQS cells. In the second part (loop on the right), bulk structures and slab cuts for a subset of the identified ground states are subjected to strain around equilibrium volumes, and the NNP (dark green rectangle) is used to either run NVT-MD or fixed-volume relaxations. A comparison of energy and force predictions is made with another variable-configuration NNP (light green rectangle) of slightly different hyperparameters (committee of two NNP models) to sample extrapolative structures and iteratively update the data set until convergence is achieved.

large-scale vacancy diffusion Monte Carlo (MC) simulation to emphasize the impact of lateral compressive strains in catalyzing the formation of vdW gaps within non-vdW  $\text{Cr}_2\text{S}_2$  slabs, paving a straightforward route for more facile exfoliation of ultrathin  $\text{Cr}_2\text{S}_2$  nanosheets through strain engineering (Results, Section 3.3). The NNP's capacity to handle lattice strains, optimize atomic positions, and accurately consider spatially and temporally diverse nonstoichiometric compositions in large-scale simulations highlights the necessity of employing MLPs for modeling nonstoichiometric systems prevalent during chemical exfoliation of non-vdW materials. This task is unachievable solely with DFT and prone to considerable inaccuracies when attempted with conventional CE methods.

## 2. METHODS

**2.1. NNP Model Workflow.** Figure 1 depicts the workflow employed for the construction of the NNP model, with comprehensive methodological details provided in the following subsections. The data set generated through this workflow is summarized in Table S1. The NNP fitting procedure consists of two principal steps. First, a CE Hamiltonian is iteratively fitted to SQS cells (referred to as  $N_{\text{SQS cells}}$  in Table S1) generated for distinct vacancy concentrations within the Cr sublattice of the stoichiometric  $\text{Cr}_2\text{S}_2$  hexagonal NiAs-type structure (space group  $P6_3/mmc$ ). Thus, these structures can be represented by the formula  $\text{Cr}_{(1-x)}\text{S}$ , where  $x$  denotes the Cr vacancy concentration. In this context, the Cr/vacancy sites are regarded as the active sites capable of accommodating two different species, while the S sites exclusively act as “spectators” within our model. The CE method, known for its simplicity and efficiency in sampling low-energy SQS cells that converge toward ground states, acts as an auxiliary model for exploring the structural space across various compositions before implementing the NNP. During CE fitting, DFT relaxations are conducted, and structural

snapshots (denoted as  $N_{\text{SQS structs}}$  in Table S1) are sampled using a farthest point sampling (FPS) algorithm to ensure more uniform sampling along the relaxation path.<sup>65,66</sup> These snapshots are then used to train a primary NNP model. This approach ensures that the NNP is trained on the equilibrium properties of the diverse atomic arrangements observed from the CE-sampled SQS cells regardless of their relative energies, with respect to the ground state.

Second, for an approximately uniform sample of these compositions, the identified ground-state SQS cells are isotropically strained around the equilibrium volume. Subsequently, the NNP is utilized to perform volume-constrained energy minimization or conduct constant-temperature, constant-volume (NVT) molecular dynamics (MD) simulations. The NNP model is updated iteratively by selecting structural snapshots (referred to as  $N_{\text{GS bulk}}$  in Table S1) from these calculations, using a committee of two NNP models.<sup>67,68</sup> The configuration of the second NNP is changed over iterations to introduce dynamic variability in its predictions, thereby enhancing the identification of extrapolative structures. This process helps improve the predictability of the elastic and vibrational properties for ground-state structures across different compositions. Additionally, for a few compositions near the ground-state composition ( $\text{Cr}_{0.667}\text{S}$ ), 2D slabs (denoted as  $N_{\text{GS slab}}$  in Table S1) with a thickness of 2 unit cells and varying surface terminations are generated from the ground-state bulk SQS cells and added to the data set. This augmentation enables the model to gain exposure to the atomic environments of surface atoms across different surface compositions. Further details on the fitting of the CE and NNP models are presented in Tables S2 and S3, respectively. To evaluate the predictive capability of the NNP, the root-mean-square error (RMSE) is reported for both energies and forces, using an 80/20 train/test data set split. For CE, we provide both the energy RMSE obtained through training on the entire SQS data set, as well as the N-fold cross-validation score,

where  $N$  denotes the number of distinct SQS cells in the data set. After validation, both the final NNP and CE models are trained on their respective complete data sets to include all available data points.

**2.2. DFT Calculations.** We use DFT for both the training and validation of the CE and NNP models.<sup>69</sup> DFT calculations are performed within the generalized gradient approximation by Perdew, Burke, and Ernzerhof (PBE), using the projector augmented-wave pseudopotentials implemented in the plane-wave Vienna ab initio simulation package.<sup>70–72</sup> Collinear spin-polarized calculations are adopted with a plane-wave basis cutoff at 350 eV, and the integration on the first Brillouin zone is carried out on uniform Monkhorst–Pack meshes with a meshing density of 4000  $k$ -points per reciprocal atom.<sup>73</sup> The electronic self-consistent loop is terminated if the energy change is less than  $1 \times 10^{-5}$  eV.

**2.3. NNP Model Fitting.** We employ the n2p2 NNP package<sup>74,75</sup> for training our NNP model. The large-scale atomic/molecular massively parallel simulator (LAMMPS) is used to perform local structural relaxations and MD simulations, using the fitted NNP as an input potential through the n2p2-LAMMPS interface.<sup>75,76</sup> The alloy theoretic automated toolkit (ATAT) tools are utilized for fitting the CE model and enumeration of the SQS cells.<sup>77–79</sup>

We adopt the Behler–Parrinello high-dimensional NNP approach.<sup>27</sup> This approach assumes that the total energy,  $E$ , of a structure can be represented as the sum of individual atomic energy contributions from constituent atoms. For our binary Cr–S system, this can be expressed as the sum of atomic energy contributions for the elements Cr and S.

$$E = \sum_{i=1}^{N_{\text{Cr}}} E_i(\mathbf{G}_i) + \sum_{i=1}^{N_{\text{S}}} E_i(\mathbf{G}_i) \quad (1)$$

The atomic energies,  $E_i$ , are generated by a set of feed-forward atomic neural networks (NNs).  $E_i$  is a function of the local environment descriptor vector  $\mathbf{G}_i$ , which features the atomic neighborhood within a given cutoff radius around atom  $i$  and constitutes the input layer of the atomic NN. Specifically, our model comprises two distinct atomic NNs: one designed for Cr atoms and another for S atoms. The  $\mathbf{G}_i$  vectors are constructed using the Behler–Parrinello symmetry functions (SFs) as descriptors.<sup>80</sup> The SFs consist of a radial function comprising sums of two-body Gaussians and an angular function incorporating additional sums of three-body terms.

$$\mathbf{G}_i^{\text{rad}} = \sum_{j \neq i} e^{-\eta(r_{ij}-r_s)^2} f_c(r_{ij}) \quad (2)$$

$$\begin{aligned} \mathbf{G}_i^{\text{ang}} &= 2^{1-\zeta} \sum_{\substack{j, k \neq i \\ j < k}} (1 + \lambda \cos \theta_{ijk})^\zeta \\ &\times e^{-\eta(r_{ij}^2 + r_{ik}^2)} f_c(r_{ij}) f_c(r_{ik}) \end{aligned} \quad (3)$$

Both SFs are many-body functions; they depend on the positions of all atoms within a cutoff radius,  $r_c$ . We used a cubic hyperbolic tangent cutoff function,  $f_c$ . The cutoff radii for radial and angular SFs, as well as the atomic NN architecture in our NNP model, are summarized in Table S3. Hyperbolic tangent is used as the activation function for hidden nodes, while the identity function serves as the activation function for the output layer.

The hyperparameter  $\lambda$  is set to  $\{1, -1\}$ , which shifts the maxima of the cosine function between  $\theta_{ijk} = 0^\circ$  and  $\theta_{ijk} = 180^\circ$ .<sup>80</sup> The  $\zeta$  values are set to  $\{1, 4, 24\}$  to cover multiple angular resolutions. Our SFs are centered at the central atom (i.e.,  $r_s = 0$ ). The radial space around the central atom is smeared by six different values of the hyperparameter  $\eta$ , which controls the radial resolution (Gaussian width). The  $\eta$  values are determined using the Imbalzano method:  $\eta_m = \left(\frac{n^{m/n}}{r_c}\right)^2$ , where  $n = 5$  and  $m = 0, 1, \dots, n$ .<sup>81</sup>

The NNP weight optimization employs an adaptive Kalman filter, updating weight parameters with each energy or force component independently as individual pieces of information.<sup>74</sup> Forces are obtained as the analytical negative gradient of the energy function. Due to the abundance of force components compared to total energy entries, training is performed in each epoch on a pattern containing total energies of all structures and only a randomly selected fraction of forces. The optimal composition corresponded to force updates of approximately 2.6 times the number of energy updates in each epoch. The NNP training procedure selects structures randomly but prioritizes more informative ones for weight updates. A structure is considered informative if its prediction error exceeds the current training RMSE by 2%. As the RMSE decreases during training, the threshold for accepting structures becomes lower, and the NNP starts accepting less important structures from the data set.

**2.4. Training Data Generation.** The structure generation for our workflow follows these steps:

#### 1 SQS cell relaxation

We sample a representative subset of structures from the DFT relaxation trajectories generated for the 243 SQS cells sampled by CE. The FPS algorithm based on DFT energies of ionic steps is utilized to remove highly similar structures, retaining approximately 70% of the original trajectory. The counts of relaxation snapshots for each of the training compositions are listed in Table S1 under  $N_{\text{SQS strucs}}$ .

#### 2 Bulk ground states

For half of the training compositions, isotropic strain is applied to the bulk ground-state unit-cell structures, varying their lattice parameters by  $\pm 10\%$ . Subsequently, the NNP is used to relax the atomic positions of the strained structures while keeping the cell volume fixed. Specific structural snapshots are then chosen for self-consistent DFT calculations, employing a committee of two NNPs. These two NNPs differ slightly in configuration and the random seed used during the stochastic training process, as well as in the train/test data set splitting.<sup>74</sup> Whenever large discrepancies between the NNPs' energy and force predictions are observed, the corresponding structures are selected for DFT calculations, leading to data set updates.

Moreover, the NNP is utilized to perform NVT-ensemble MD simulations for  $2 \times 2 \times 2$  supercells of the ground-state structures at three compositions close to the ground-state composition (Cr<sub>0.667</sub>S), specifically, Cr<sub>0.7</sub>S, Cr<sub>0.625</sub>S, and Cr<sub>0.5</sub>S. The MD trajectories encompass various temperatures (300, 600, and 900 K) at isotropically strained volumes ( $\pm 5$  and  $\pm 10\%$  strain in lattice constant), in addition to the equilibrium volume. Similarly, snapshots are selected from the MD trajectories employing a two-NNP committee, ensuring that each pair of successively selected snapshots is separated by at

least 100 fs to minimize statistical correlations. The number of bulk ground-state snapshots generated using both the strain/relax and strain/MD approaches is recorded for the respective compositions in column  $N_{\text{GS bulk}}$  of Table S1.

### 3 Slab cuts of ground states

We generate two-unit-cell-thick slab structures for the ground states at the three lowest-energy training compositions:  $\text{Cr}_{0.7}\text{S}$ ,  $\text{Cr}_{0.667}\text{S}$ , and  $\text{Cr}_{0.625}\text{S}$ . First, the bulk unit cell is shifted incrementally along a randomly chosen cell vector; then, a vacuum layer larger than 15 Å is added in the direction of that cell vector to create 2D slabs with diverse surface terminations across the crystal. These slabs are subjected to  $\pm 5\%$  strain around equilibrium and then fully relaxed using the NNP model. Structural snapshots are sampled from the relaxation trajectories using the NNP committee method, followed by self-consistent DFT calculations and data set updates. The number of slab structures generated for each composition is recorded in column  $N_{\text{GS slab}}$  of Table S1.

Figure S4 presents a reduced-dimensionality representation of the feature space spanned by the atomic environments in the above data set, providing a means to evaluate structural similarities between the different structures comprising the data set. The above DFT data set comprised a total of 10,593 structures. In addition, for Sections 3.2 and 3.3 in the Results section, we augmented our training set with 380 structures sampled by FPS from the fixed-cell-volume relaxation trajectories of the vdW  $\text{CrS}_2$  bulk unit cell. These structures were rendered at various isotropic compressive strains ranging from 0 to 10% along each lattice vector, with increments of 2%. This augmentation was done to particularly enhance the accuracy of NNP predictions at high compressive strains of  $\text{CrS}_2$ .

**2.5. Simulated Annealing.** The SA procedure employed for crystal structure optimization, as detailed in Results, 3.2, commences with the system's initial equilibration at a high enough temperature ( $T = 21,000$  K), which enables a relatively unrestrained exploration of the configurational space. Subsequently, the system undergoes a gradual cooling process (following a geometric sequence) consisting of 50,000 steps (which is found sufficient for our supercells to achieve energy convergence), culminating in the convergence toward a local minimum at a relatively low temperature ( $T = 0.01$  K). This cooling strategy facilitates occasional uphill moves in the early stages, prompting an exhaustive search for low-energy basins on the potential energy surface (PES). To enhance the exploration of the low-energy crystal structures, we introduce a cyclic restart strategy, consisting of 12 cycles, into our SA workflow. At the conclusion of each cycle, the temperature is reset to a value of 1000 K lower than the initial temperature, thereby inducing diverse cooling rates and promoting a more thorough exploration of the low-energy crystal structures. Each iteration during SA involves either the exchange of two random groups of vacancies and Cr atoms (88% of total steps) or the perturbation of lattice parameters of the simulation cell (12% of total steps) to maintain a zero-mean pressure. In the case of cell perturbations, the atomic positions are scaled with the stretched lattice to preserve fixed fractional coordinates, and the energies are computed using the NNP statically (without further relaxation of positions). The acceptance or rejection of these moves adheres to the Metropolis criteria for the isobaric–isothermal (NPT) ensemble. Following this, the NNP model is employed to conduct full structural relaxations

toward the neighboring local minima for the set of distinct configurations derived from the SA cycles. This endeavor aims to accurately discern the ground-state configuration amidst various alternative metastable structures.

**2.6. Vacancy Diffusion Monte Carlo.** The MC simulations utilized for modeling Cr vacancy diffusion during non-vdW to vdW phase transformation in  $\text{CrS}_2$  slabs, as discussed in Section 3.3, are conducted in the NPT ensemble, maintaining a temperature of 300 K and zero absolute pressure in the  $z$ -direction. Starting with a randomized Cr/vacancy distribution in the Cr sublattice, each MC step involves either a perturbation in the slab thickness (12% of total steps) or a proposal for a group of randomly chosen vacancies to move to any of their nearest neighbor (nn) sites in the Cr sublattice (88% of total steps). The nn list includes the surrounding six Cr sites in a hexagonal arrangement within the same plane, as well as the analogous seven sites in each of the upper and lower Cr layers, as illustrated in Figure 6a. Each step of vacancy diffusion can be conceptualized as either remaining within the same layer or executing a vertical jump to an adjacent Cr layer, subsequently choosing to either stay at the new site or execute a horizontal movement to a nn in the new layer. This results in equal probabilities for movements in the  $x$ – $y$  plane and along the  $z$ -direction, ensuring unbiased vacancy transitions within the slab. During the MC simulation, we utilized an exponential growth function to adjust the number of permissible minimization steps, wherein the rate decreases in proportion to the MC steps. After conducting multiple tests with different rates and maximum values, we settled on the function  $80 \times e^{(-\text{step}/10^5)}$  to achieve a nearly zero mean pressure with minimal fluctuations in the  $z$ -direction. Thus, this choice minimizes the forces on atoms while ensuring a steady-state equilibrium of the slab with the surrounding environment in the  $z$ -direction, along which the slab is exposed to a vacuum. The MC simulation is terminated when a reduction of less than 1 meV/atom in the cohesive energy of the slab is observed over a period of 10,000 steps, resulting in a total of 210,000 steps (see Figure 6c).

## 3. RESULTS

**3.1. Generalization of NNP for Nonstoichiometric Crystal Structure Optimization.** Crystal structure optimization in the context of nonstoichiometric solids typically involves two primary aspects: (i) configurational optimization, which involves determining the equilibrium arrangement of vacancies on the lattice sites and (ii) local geometric optimization, which pertains to the local adjustment of structural parameters such as atomic positions and cell dimensions. Different vacancy configurations can be visualized as distinct basins on the PES, while the geometrically relaxed structures represent the local minima within these basins. While addressing both configurational and geometrical optimizations is crucial in global optimization problems, it is often reasonable to restrict this coupling to the low-energy basins within the PES.<sup>17,82</sup> This approach is warranted by the constrained influence of local geometrical optimization on the energy of unfavorable configurations, attributed to the presence of barriers between the distinct basins. Thus, a configuration that hinders the formation of stable bonds is highly likely to persist as a high-energy structure, even after undergoing geometrical optimization.

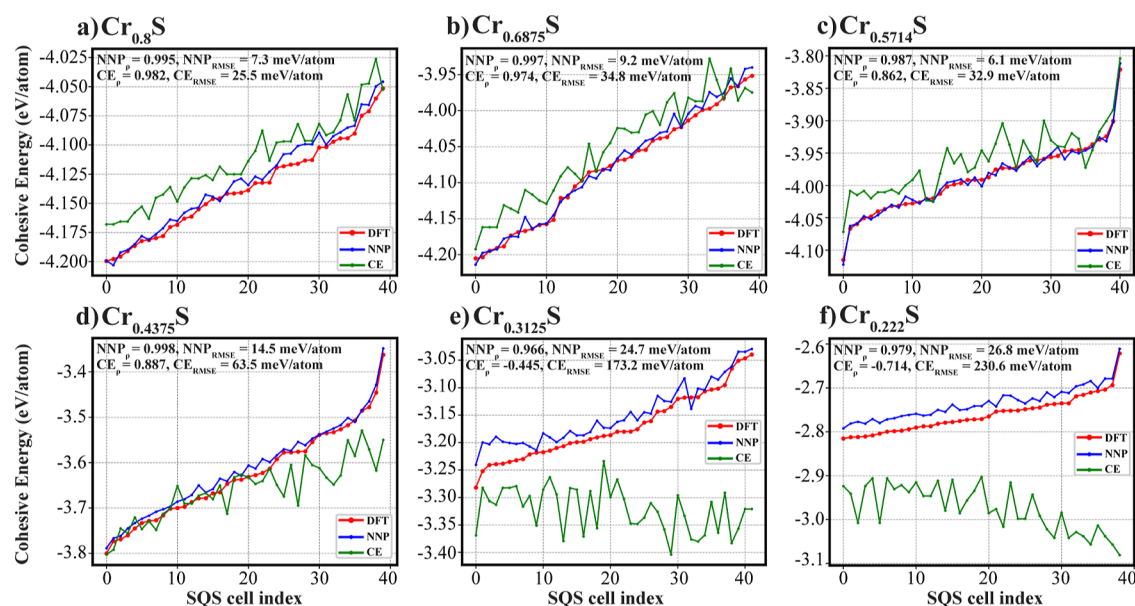


**Figure 2.** Evaluation of the NNP for configurational optimization at unseen compositions. The ranking of around 40 SQS cells, at six different unseen compositions, is demonstrated using CE, NNP, and DFT. The depicted ordering is based on the DFT energies, as observed from the monotonically rising DFT energy with the cell index. The SQS cells span the entire energy range of the enumerated SQS cells (<48 atoms per cell).

To evaluate the crystal structure prediction capability of our NNP model at different compositions, we initially assess its ability to rank on-lattice configurations with different vacancy arrangements across various unseen compositions. By decoupling the off-lattice local geometrical optimization from the on-lattice configurational optimization (which is the strength of the CE method), we enable more meaningful comparisons between the NNP and CE models. Subsequently, we examine the NNP model's ability to accurately reproduce energies and forces for the lowest-energy configurations subjected to elastic strains and atomic perturbations from lattice sites. By successfully reproducing these energy and force profiles, we can validate the NNP model's effectiveness in fitting the PES around the local minima of low-energy basins, thus showcasing its competence in performing local geometric optimization.

**3.1.1. Configurational Optimization.** To minimize the cost associated with the data set generation during the training of the NNP model, we limited our consideration to small SQS cells with fewer than 20 atoms during CE sampling. As a result, the composition space in the DFT data set used for training/validating the NNP model was restricted to the 22 compositions outlined in Table S1. In order to broaden the range of compositions accessible for assessing the NNP generalization, we increased the maximum number of allowable atoms per SQS cell from 20 (as used in CE sampling) to 48. This enables us to accommodate a wider spectrum of elemental proportions of Cr and S atoms. Subsequently, we select a new set of 18 unseen vacancy compositions to validate the generalization of our model. To ensure a comprehensive assessment of the NNP model's ability to explore the entire configurational space for these unseen compositions, we opt for an exhaustive approach instead of employing any form of configuration sampling. This involves enumerating all possible SQS cells for the chosen compositions. The pool of enumerated SQS cells for the new 18 compositions encompassed approximately 130,000 symmetrically distinct configurations. Next, we employed the NNP model to rank the enumerated SQS cells at each composition

based on their cohesive energies. Initially, the energies of all SQS cells were statically computed without relaxation. Then, for the 300 SQS cells with the lowest energies at each composition, a full relaxation procedure was implemented. This correction step aimed to rectify any potential inaccuracies in the ranking of the low-energy configurations caused by the initial constraint on the geometrical degrees of freedom.

Among the numerous SQS cells available for each composition, we purposefully selected a subset of around 40 configurations. These configurations are chosen to span the entire energy range with approximately equal intervals. In order to ensure a fair comparison between the NNP and CE models, we use here a second CE model fitted to the DFT energies of the SQS cells in the data set, computed statically on-lattice without relaxation. This approach helps to eliminate any potential bias that may arise from the first CE model which was trained on DFT energies of fully relaxed SQS cells and then utilizing it for predicting the energies of on-lattice configurations. The comparison of the NNP and CE models against DFT is illustrated in Figure 2, focusing on six representative unseen compositions. The accuracy of each model is assessed using two key metrics: Spearman's rank-order correlation coefficient,<sup>83</sup> denoted as  $\rho$ , which measures the degree of similarity in the energy-based ranking order of SQS cells, and RMSE, which quantifies the discrepancy between the predicted and actual energies.

As illustrated in Figure 2, the NNP demonstrates superior performance compared to CE, yielding RMSE values akin to those obtained during training/test evaluation (refer to Table S3), with all  $\rho$  values exceeding 0.96. Nevertheless, a slight reduction in performance is noted for  $\text{Cr}_{1-x}\text{S}$  configurations with a vacancy concentration,  $x$ , above  $\sim 0.55$  (as can be noticed from Figure 2f). However, this can be deemed acceptable for such elevated vacancy concentrations which typically correspond to experimentally infeasible structures. Even if these structures are encountered in theoretical simulations, they are likely to be rejected due to their inherent instability. Conversely, CE exhibits a performance comparable

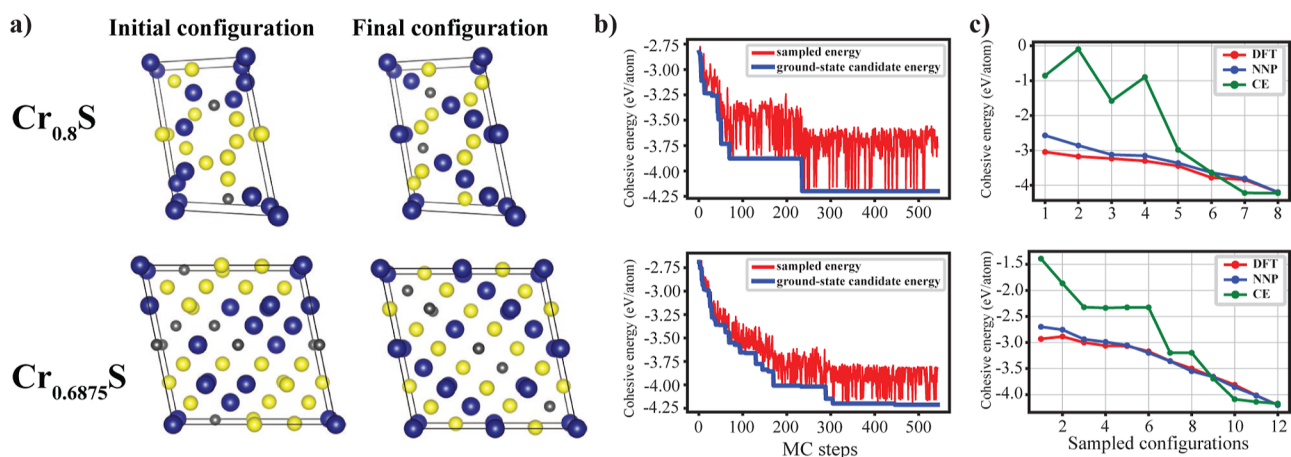


**Figure 3.** Generalization of the NNP for extrapolative sublattice configurations. (a) Chemical order of the ground-state configuration is initially randomized for two unseen compositions ( $\text{Cr}_{0.8}\text{S}$  and  $\text{Cr}_{0.6875}\text{S}$ ), allowing any species (Cr, S, or vacancy) to occupy any site (not constrained to the training Cr/vacancy and S sublattice partitioning). (b) NNP is utilized to perform short MC simulations involving atomic swaps until the ground state is retrieved. (c) Different configurations are sampled from the MC trajectory at nearly uniform energy intervals and subsequently validated against CE and DFT.

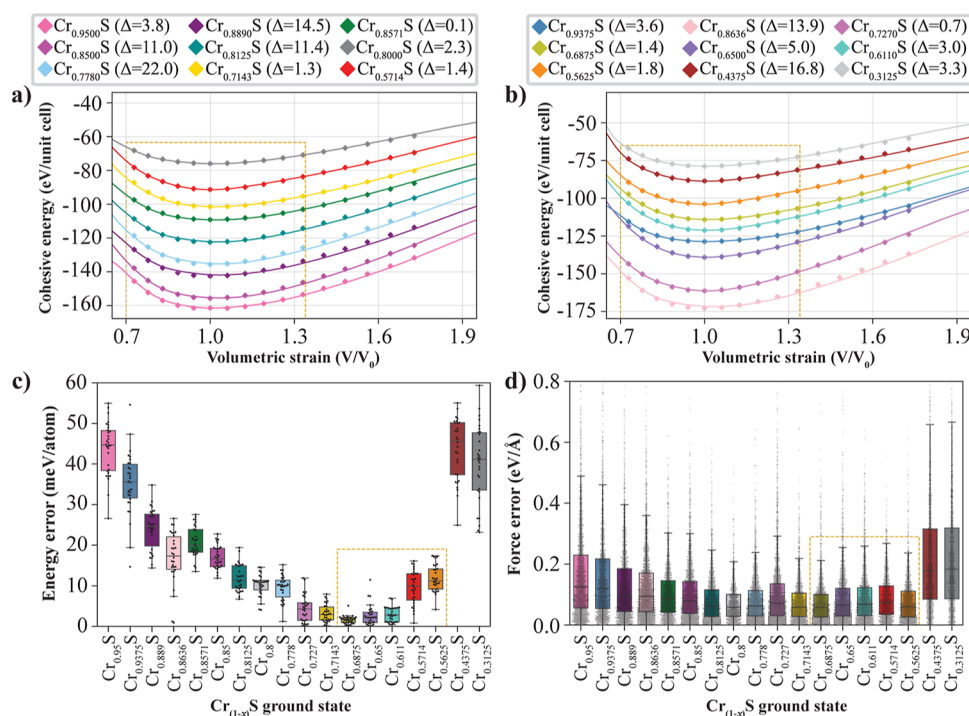


**Figure 4.** Generalization of the NNP for elastic and vibrational perturbations of ground-state structures at unseen compositions. (a,b) Cohesive energy vs volumetric strain curves as predicted by NNP (solid lines) compared to DFT reference values (discrete markers). The structures are divided between panels (a) and (b) for clarity. Numerical error estimations of NNP predictions are provided by the listed  $\Delta$  values (in meV/atom) for each structure. The dashed yellow boxes in (a,b) indicate the volumetric strain range that NNP witnessed for some training structures. (c,d) Box plots for NNP energy and force error distributions based on 30 snapshots sampled from 500 K MD simulations at 3 ps intervals. The rectangular box indicates the interquartile range (IQR), while the line within the box represents the median. The dashed yellow boxes in parts (c,d) specify the composition range over which NNP was trained on high-temperature configurations of ground-state structures (specifically at  $\text{Cr}_{0.7}\text{S}$ ,  $\text{Cr}_{0.625}\text{S}$ , and  $\text{Cr}_{0.5}\text{S}$ ).

to that of NNP, albeit to a lesser degree, for compositions that span relatively low energies; however, the performance deteriorates significantly for high-energy compositions, where the model entirely loses its ability to rank the different configurations for vacancy concentrations beyond  $x \sim 0.55$ . The notable advantage of the NNP over CE, despite both models being trained on the same configurational arrangements (i.e., the same SQS cells), highlights the greater

flexibility of the NNP in effectively generalizing to diverse crystal structures with varying chemical occupations and compositions.

Nonstoichiometric systems are typically treated by using sublattice models. Accordingly, we partitioned the parent stoichiometric  $\text{Cr}_2\text{S}_2$  lattice into two sublattices: a sublattice of active sites (Cr, vacancy) and another sublattice of inactive S sites, in accordance with experimental observations. All of the

SQS cells employed in training and validation were constrained within this partitioning. Despite the rationality of this sublattice approach, it is of interest to investigate the ability of the NNP to generalize to arbitrary chemical occupations, where each species (Cr, vacancy, and S) can occupy any site in the cell. In this context, we select the ground-state SQS cells identified for two unseen compositions,  $\text{Cr}_{0.8}\text{S}$  and  $\text{Cr}_{0.6875}\text{S}$ , and then randomize the chemical occupation in each cell to generate initial disordered configurations, as depicted in Figure 3a. Subsequently, we conduct simple MC simulations using the NNP. In each step, an MC swap of two sites of different species is randomly suggested, and a greedy algorithm is employed to accept or reject the move. The NNP model successfully restores the ground-state configurations, as shown in Figure 3b, demonstrating its accurate ranking capability by rejecting highly energetic configurations until reaching the true ground state. Furthermore, we sampled a number of configurations from the MC trajectories at nearly equal energy intervals and calculated their DFT energies. From Figure 3c, it is evident that the performance of the NNP retains its high quality even for highly randomized configurations with cohesive energies above  $\sim -4$  eV/atom, which is roughly the highest energy observed for the SQS cells of the two considered compositions ( $\text{Cr}_{0.8}\text{S}$  and  $\text{Cr}_{0.6875}\text{S}$ ) when S atoms were considered inactive (see Figure 2). Only in the vicinity of the highest energy configurations does the deviation of NNP-predicted energies start to increase; however, the ranking predictions remain in very good agreement with DFT throughout the entire energy range. On the other hand, CE successfully identifies the random configurations as unfavorable with high-energy predictions, albeit with considerably higher error values compared to the NNP. The overall remarkable capability of the NNP to accurately rank unseen configurations across a broad spectrum of energies and diverse compositions underscores its robustness as a promising tool to drive MC simulations and generate more reliable trajectories for atomic diffusion processes.

**3.1.2. Local Geometrical Optimization.** The preceding part elucidated the ability of the NNP to exhibit generalization across various atomic configurations, covering the space of SQS cells across a wide range of compositions. Here, we analyze the efficacy of NNP to approximate the PES in the vicinity of local minima corresponding to ground-state structures at different compositions. Specifically, we focus on the lowest-energy SQS cells at 18 unseen compositions, as determined by the NNP from the enumerated SQS cells.

To evaluate the performance of NNP at various bond lengths that significantly deviate from equilibrium, we subject the relaxed ground-state configurations to isotropic strain ranging from  $-10$  to  $+20\%$  along each lattice vector, with an increment of 2%. Panels a and b in Figure 4 illustrate the NNP predictions of cohesive energies at these volumetric strains for the ground-state structures associated with the 18 unseen compositions. The NNP predictions are computed over a fine-grained grid of strains, visually represented by solid lines in the figure. The discrete markers, on the other hand, represent the reference values obtained from DFT, revealing a remarkable concurrence with the NNP predictions across a wide range of test volumes and varying compositions. It is noteworthy that the error in the NNP predictions remains relatively uniform throughout the strain range, albeit with a slight increase observed at extreme strains. In order to provide a quantitative assessment of the accuracy achieved by the NNP, we utilize a

measure,  $\Delta$ , which is commonly employed to compare equations of state derived from different models.<sup>84–86</sup>

$$\Delta = \frac{\int_{(0.9)^3 V_0}^{(1.2)^3 V_0} |E^{\text{NNP}}(V) - E^{\text{DFT}}(V)| dV}{((1.2)^3 - (0.9)^3) V_0} \quad (4)$$

where the  $E^{\text{NNP}}(V)$  and  $E^{\text{DFT}}(V)$  functions are obtained by fitting a sixth-order polynomial to the corresponding data,  $V_0$  denotes the equilibrium cell volume, and the 0.9 and 1.2 values correspond to the  $-10$  and  $+20\%$  applied strain to each lattice vector. The  $\Delta$  value for each composition is outlined (in meV/atom) at the top of Figure 4a,b. It can be observed that two-thirds of the  $\Delta$  values are below the estimated RMSE of the NNP (refer to Table S3), while the largest error of 22.0 meV/atom is about 2.5 times that value. It should also be noted that the NNP was trained on strained ground-state structures associated with training compositions (referred to as  $N_{\text{GS bulk}}$  in Table S1), where the volumetric strain during training was limited to the range from 0.73 to 1.33 times the equilibrium volumes. Nevertheless, NNP still matches DFT values for larger strains up to 1.73 of the equilibrium volumes. However, we observe larger deviations when attempting to extrapolate to volumetric strains smaller than 0.7. This can be attributed to the relatively higher forces associated with such large compression strains, which the NNP model might not have been sufficiently trained to accurately capture and represent.

Next, we focus on the capacity of the NNP to accurately replicate the energies and forces obtained from DFT during MD simulations. This aspect is of considerable importance as it directly influences the model's proficiency in accurately relaxing atomic positions and predicting vibrational properties. In this retrospect, we run NNP-driven MD simulations for the relaxed unit cells of the 18 test structures at 500 K with a 0.5 fs time step. Then, we sample 30 snapshots from the MD trajectory and perform self-consistent DFT calculations to verify the energies and forces on the sampled structures. To mitigate correlations between the sampled structures, we adjust the time interval between each two successively sampled snapshots to 3 ps. Panels c and d in Figure 4 demonstrate the error distribution of energies and forces across ground-state structures of the 18 compositions. It is worth noting that the NNP has been trained only on high-temperature MD configurations for  $\text{Cr}_{0.7}\text{S}$ ,  $\text{Cr}_{0.625}\text{S}$ , and  $\text{Cr}_{0.5}\text{S}$  ground states. Despite this, we observe that the median energy error is below 20 meV/atom for structures ranging from  $\text{Cr}_{0.8636}\text{S}$  to  $\text{Cr}_{0.5625}\text{S}$ . A similar behavior is observed for force errors, where we can see that the medians of force errors are below 0.2 eV/Å for all compositions, and aside from a few outliers, the full distributions of force errors are smaller than 0.3 eV/Å in the composition range from  $\text{Cr}_{0.8636}\text{S}$  to  $\text{Cr}_{0.5625}\text{S}$ . This reveals the interpolation ability of the NNP, allowing it to accurately approximate the vibrational properties of ground-state structures at unseen compositions. Although the NNP exhibits a good extrapolation ability outside the training composition range, even beyond the compositions used in high-temperature MD training ( $\text{Cr}_{0.7}\text{S}$ ,  $\text{Cr}_{0.625}\text{S}$ , and  $\text{Cr}_{0.5}\text{S}$ ), we speculate that this behavior is primarily captured from training on the relaxation structures of nearby training compositions. Consequently, we observe a gradual increase in energy and force errors as we deviate away from the composition range that comprised the high-temperature MD training (denoted by the yellow box in Figure 4). This occurs because, for these

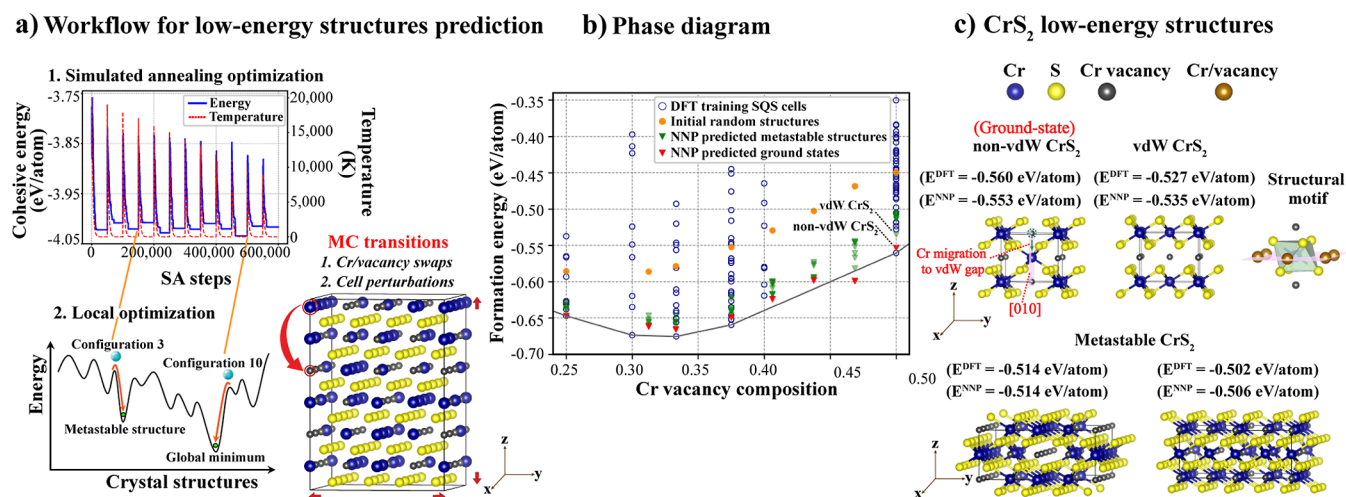


**Figure 5.** Simulated annealing prediction of  $\text{Cr}_{(1-x)}\text{S}$  stable structures: (a) NNP-driven crystal structure prediction workflow: (1) 12-cycle simulated annealing (SA) with Cr/vacancy swaps and cell perturbations. The represented structure illustrates the allowed MC transitions (red arrows) in the adopted supercell during SA; (2) local geometry relaxations of the candidate configurations to identify global minimum from metastable structures. (b) Schematic of the phase diagram of  $\text{Cr}_{(1-x)}\text{S}$  in the range  $x = [0.25, 0.5]$  along with the identified ground states and metastable structures. (c) Refined cells of the ground state and few metastable structures for the  $\text{CrS}_2$  phase.

compositions, the energy and force predictions are solely reliant on similarities to the training relaxation structures sampled at the proximate compositions. To provide similarity measures between the unseen structures utilized for assessing the configurational and geometrical generalization of the NNP model, we present in Figure S5 a comparison between the reduced-dimensionality representation of the feature space spanned by the atomic environments in these structures and those in the DFT data set.

**3.2. Crystal Structure Predictions for  $\text{Cr}_{(1-x)}\text{S}$ .** The characterization of material properties, encompassing the electronic band structure, density of states, and magnetic characteristics, exhibits a profound reliance on the fundamental crystalline framework (comprising atomic occupations and positions). It is imperative to ensure a precise representation of the input crystal structures in order to enhance the predictive capacity of DFT in property prediction, as any deviations from realistic structures may introduce uncertainty into the property predictions.

In this subsection, we implement the NNP model to accurately explore the low-energy  $\text{Cr}_{(1-x)}\text{S}$  crystal structures across different compositions. To achieve this, we utilize the SA algorithm, a well-established and robust optimization technique in the field of crystal structure optimization.<sup>17,87,88</sup> To enhance the exploration of the low-energy crystal structures, we incorporate a cyclic restart strategy (comprising 12 cycles) within our SA workflow, yielding an ensemble of up to 12 distinct Cr/vacancy configurations and ensuring a trade-off between diversity and computational efficiency. The SA procedure is illustrated in Figure 5a, and additional details can be found in the “Methods” section.

In this study, we limit our SA work to identifying the low-energy  $\text{Cr}_{(1-x)}\text{S}$  structures in the vacancy concentration range ( $0.25 \leq x \leq 0.5$ ), aligning with experimental interest. We choose 8 different compositions to sample this range. To encompass a diverse set of compositions, we employ  $4 \times 2\sqrt{3} \times 3$  supercells, which are derived from the orthorhombic ( $Pnmm$ )  $\text{Cr}_2\text{S}_2$  conventional unit cell (see Figure S1). This supercell size of lattice parameters in the range of 12.0 to 16.0 Å allows us to strike a balance between mitigating

finite-size errors and ensuring appropriately sized unit cells for future DFT investigations. Figure 5b illustrates the comprehensive phase diagram of  $\text{Cr}_{(1-x)}\text{S}$  across the range of compositions under investigation. The diagram presents formation energies, computed with reference to the most thermodynamically stable phases of Cr and S elements as available in the Materials Project database,<sup>89</sup> namely mp-90 (Cr in BCC lattice) and mp-96 (S in  $P2/c$  space group), respectively. The depicted energies encompass the NNP-predicted values for both the initial random configurations at 0th step of each SA process and the distinct low-energy structures, including both ground states and metastable configurations, obtained for the 8 considered compositions. Additionally, the diagram includes the DFT formation energies of the SQS cells present in the NNP training set within the same composition range. The applied workflow effectively identified the ground-state ordered structures corresponding to all known phases in the considered composition range, namely  $\text{Cr}_{0.75}\text{S}$  ( $\text{Cr}_3\text{S}_4$ ) (mp-964),  $\text{Cr}_{0.667}\text{S}$  ( $\text{Cr}_2\text{S}_3$ ) (mp-555569), and  $\text{Cr}_{0.375}\text{S}$  ( $\text{Cr}_3\text{S}_8$ ) (mp-1181961) (see Figures S2 and S3). This validation confirms the precision and reliability of both the NNP model and the SA workflow in predicting ground-state structures.

Notably, a consistent observation within the investigated composition range reveals a pronounced preference for ground-state structures that feature complete  $\text{CrS}_2$  layers intercalated by Cr-deficient layers (see the predicted ground states and the layer occupation distributions in Figure S2). This intriguing finding indicates a tendency for vacancies to aggregate, forming alternating ( $\text{CrS}_2$  and Cr-deficient) layers rather than being uniformly distributed across all layers. Hence, the presence of  $\delta$  excess intercalant Cr atoms above the  $\text{Cr/S} = 1/2$  ratio (i.e.,  $\text{Cr}_{(1+\delta)}\text{S}_2$ ) occupying the vdW gaps manifests as a critical factor in stabilizing  $\text{CrS}_2$  layers, preventing Cr migration from them into the vdW gaps, even for small  $\delta$  values down to approximately 0.03, as observed for the  $\text{Cr}_{0.53125}\text{S}$  phase. Upon reaching the  $\text{Cr}_{0.5}\text{S}$  composition, the energy cost associated with forming  $\text{CrS}_2$  layers and empty vdW gaps in-between becomes higher, leading to a compelling phenomenon where half of the Cr atoms preferentially migrate

to the vdW gaps, forming a non-vdW CrS<sub>2</sub> structure. This manifests that CrS<sub>2</sub> does not prefer the vdW nature, as already observed in experiments.<sup>7,11,13,16</sup> Figure 5c presents both the ground-state non-vdW CrS<sub>2</sub> and the subsequent stable phase, the pure vdW CrS<sub>2</sub>. The non-vdW CrS<sub>2</sub> configuration can be conceptualized as a transformation from vdW CrS<sub>2</sub>, wherein 50% of the Cr atoms undergo orderly shifts toward the vdW gap along the [010] direction, resulting in an AB stacking pattern, distinct from the AA stacking seen in vdW CrS<sub>2</sub>. The DFT formation energy of non-vdW CrS<sub>2</sub> is lower by 33 meV/atom, underscoring the non-vdW character of Cr–S systems. A more precise calculation, incorporating vibrational free-energy contributions associated with phonons, is illustrated in Figure S6. The results indicate that the free energy of the non-vdW CrS<sub>2</sub> phase is predicted to be lower for temperatures up to around 465 K, affirming its higher stability compared to that of the vdW phase. Moreover, it should be noted that the reported DFT results are obtained using the standard PBE functional without a vdW correction term. However, including a vdW correction is observed to increase the binding of the non-vdW phase more than the vdW one, thereby predicting a larger relative stability of the non-vdW phase.

Nevertheless, it is imperative to recognize that solely prioritizing the acquisition of the ground-state (global minimum) structure may be insufficient in faithfully representing the material's experimental reality. This is due to the presence of alternative low-energy local minima in the PES, which correspond to metastable phases capable of being adopted by the material during the synthesis process or through thermal excitation. This becomes particularly significant in the case of 2D non-vdW materials, such as Cr-based 2D materials, where the interlayer bonding forces between atoms are typically stronger than vdW interactions. As a consequence, rapid and uncontrolled interlayer diffusion may occur from the Cr-rich layers to the Cr-deficient layers, restricting the scope of lateral rearrangement of Cr atoms during synthesis. This phenomenon ultimately leads to the stabilization of metastable structures with smaller ranges of order, thereby hindering the material from attaining its global minimum long-range ordered crystal structure. For instance, during the soft chemical synthesis of CrS<sub>2</sub> slabs derived from bulk NaCrS<sub>2</sub> through proton exchange, the deintercalation of Na induces a notable degree of disorder within the Cr sublattice.<sup>7,11</sup> This is evident, as the Cr atoms undergo rapid and uncontrolled transitions from the CrS<sub>2</sub> (Cr-rich) layers to the vacant Na (Cr-empty) sites. As a result, a metastable CrS<sub>2</sub> structure forms, where both Cr atoms and vacancies are randomly distributed throughout the Cr-sublattice, forming a 3D chemically bonded arrangement. Figure 5c represents refined unit cells of two metastable CrS<sub>2</sub> structures observed during our SA. The metastable structures are not perfectly ordered as the non-vdW or vdW structures; however, the prominent structural motif in these two ordered structures can still be observed in the two metastable structures with higher formation energies. In particular, we can notice that each Cr atom consistently exhibits a preference for being neighbored by vacant sites in the adjacent top/bottom Cr layers, while its lateral surroundings entail a disordered disposition of both Cr atoms and vacancies. This configuration more accurately reflects both the non-vdW and disordered characteristics observed in the experimentally synthesized 2D CrS<sub>2</sub> slabs, where roughly half of the Cr atoms undergo random interlayer jumps from the CrS<sub>2</sub> layers to the vdW gaps, resulting in the

creation of randomly scattered Cr sites neighbored by vacant sites in the adjacent top/bottom Cr layers. As a consequence, these metastable structures manifest as better representative supercells enriched with more realistic motifs for the DFT property predictions. This behavior is not exclusive to CrS<sub>2</sub>, as it is also experimentally observed in other phases. For instance, the ground-state ordered phase of Cr<sub>2</sub>S<sub>3</sub> displays a structural configuration akin to CrS<sub>2</sub>–Cr<sub>1/3</sub>–CrS<sub>2</sub>, wherein Cr<sub>1/3</sub> forms Cr lines extended along the armchair direction, separated by two vacant lines in either ABC or AB stacking.<sup>8,9,90</sup> However, structural characterization of CVD-grown Cr<sub>2</sub>S<sub>3</sub> slabs reveal a pronounced degree of disorder in the Cr-deficient layers, leading to the crystal being characterized as a CrS<sub>2</sub>-disordered Cr<sub>1/3</sub>–CrS<sub>2</sub>.<sup>90</sup> The same thing applies for Cr<sub>3</sub>S<sub>4</sub>, being characterized as a CrS<sub>2</sub>-disordered Cr<sub>1/2</sub>–CrS<sub>2</sub>.<sup>90</sup>

### 3.3. Strain-Induced vdW Gaps in Non-vdW CrS<sub>2</sub> Slabs.

In the preceding sections, we discussed that Cr atoms within Cr–X structures exhibit a high propensity to migrate from the CrX<sub>2</sub> layers to partially occupy the vdW gaps,<sup>7,11,13,16</sup> thereby establishing strong 3D chemical bonds within the crystal lattice. The presence of such chemical bonds between adjacent layers in these CrX<sub>2</sub> materials poses challenges in achieving precise thickness control during the exfoliation process, limiting the attainment of ultrathin sheets down to a monolayer thickness. For the case of CrS<sub>2</sub> exfoliation, the deintercalation of Na from NaCrS<sub>2</sub>, followed by LPE typically yields sheets with a minimum thickness of approximately 2–3 nm.<sup>7,11,13</sup> Furthermore, our findings in Section 3.2 demonstrate that the ground-state structure of CrS<sub>2</sub> favors a uniform distribution of vacancies throughout the layers of bulk crystal rather than forming a vdW CrS<sub>2</sub> structure. In this section, we show that lateral compressive strain is a viable method for inducing the reconstruction of vdW gaps between the CrS<sub>2</sub> layers. This effect leads to a reduction in the interlayer interactions, thereby facilitating the exfoliation process of these materials. A similar phenomenon has been experimentally observed in other materials, such as germanium telluride, where lateral compression was found to induce the opening of vdW gaps.<sup>91</sup>

In this retrospect, we consider a symmetric CrS<sub>2</sub> slab with a S termination on both sides. The slab consists of a  $16 \times 9\sqrt{3} \times 8$  supercell of the orthorhombic (*Pnmm*) conventional unit cell (6912 atoms per simulation cell), with periodic boundary conditions applied in the *x*–*y* directions and a 30 Å vacuum layer in the *z*-direction. The *x*–*y* lattice constants are constrained to approximately 5.06 nm × 4.93 nm, while the thickness in the *z* direction is allowed to freely relax starting from an initial value of 4.18 nm. These *x*–*y* lattice constants correspond to a lateral strain of around 3.5% compared to the free-standing CrS<sub>2</sub> monolayer with a lattice constant of around 0.329 nm. This strain value is approximately half of the strain observed in CVD-grown vdW CrS<sub>2</sub> slabs on f-mica substrate,<sup>10</sup> where the lattice mismatch is approximately 7%. We consider the average strain value in the CVD-grown CrS<sub>2</sub> slabs, assuming a linear variation of strain from 7% to zero as we move away from the substrate.

Starting from a non-vdW CrS<sub>2</sub> slab with a randomized Cr/vacancy distribution in the Cr sublattice, we utilize the NNP to conduct a vacancy diffusion MC simulation within the *NPT* ensemble, at 300 K and zero absolute pressure in the *z*-direction. Throughout the MC steps, Cr atoms/vacancies undergo intralayer and interlayer diffusions to their nearest neighbors (see Figure 6a), leading to a gradual transformation

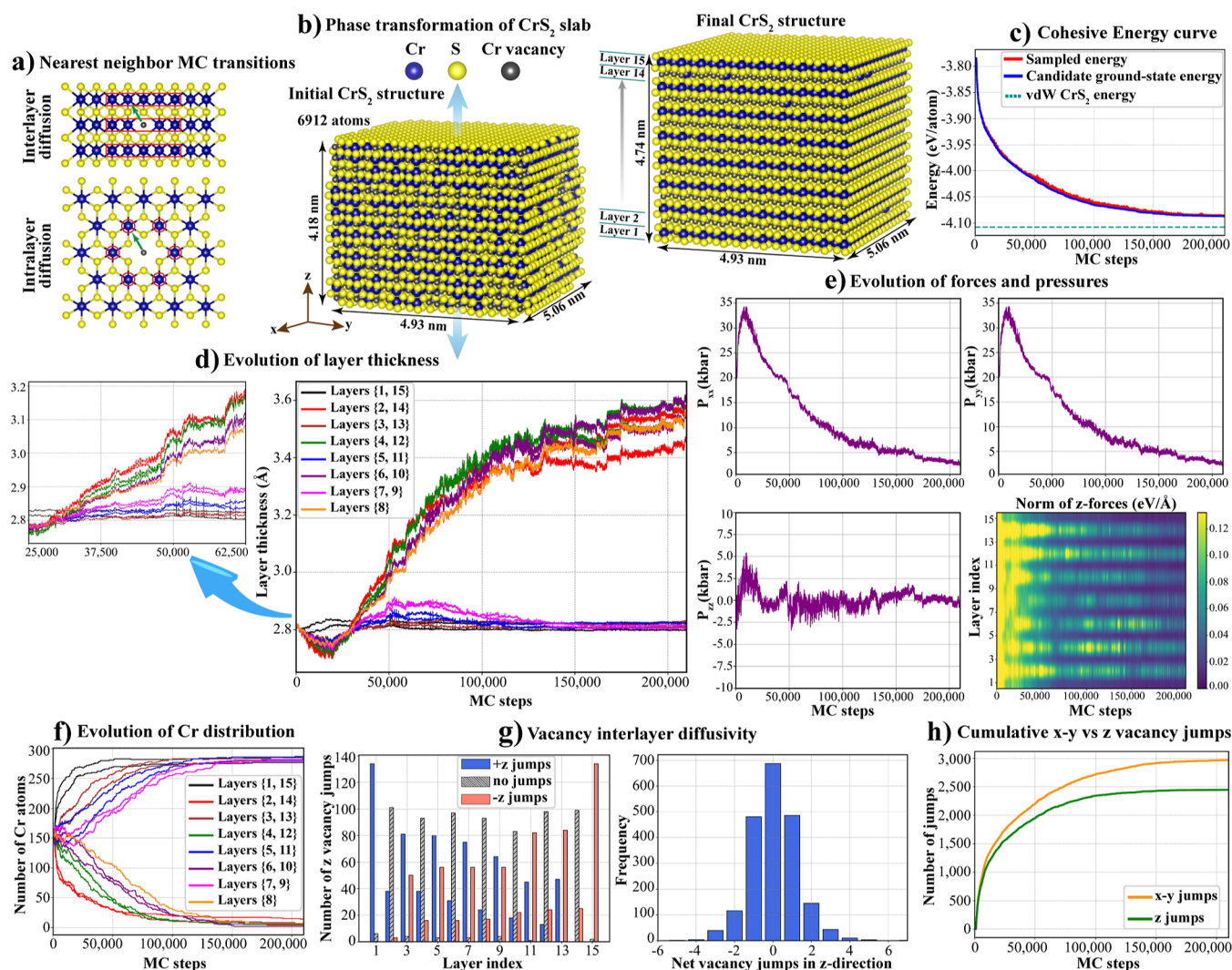


**Figure 6.** Strain-induced vdW gaps in  $\text{CrS}_2$  slabs. (a) nn vacancy transitions implemented during the MC simulation (a vacancy can jump to any of the 6 surrounding sites identified by the red circles in the same plane, or to any of the 7 nn sites in the adjacent top or bottom Cr layers). (b) Initial random configuration along with the final configuration resulting from atomic rearrangements induced by lateral compressive strain. Layer numbering is indicated in the figure. (c) Reduction in cohesive energy of the slab during the MC simulation. (d) Thickness evolution of the 15 layers over MC steps. (e) Variation in pressure tensor diagonal components besides the norm of z-forces on Cr atoms for each layer in the slab. (f) Evolution of the number of Cr atoms across the layers over MC steps. (g) Summary of the count and direction of interlayer vacancy migrations from each layer (shown in the bar plot) along with the frequencies of net interlayer jumps of all vacancies from their initial layers (shown in the histogram). (h) Cumulative numbers of interlayer and intralayer transitions made by all vacancies from their initial positions in the slab.

toward a quasi-vdW  $\text{CrS}_2$  phase. Further details of the MC simulation procedure are elucidated in the “Methods” section.

Figure 6b illustrates the initial and final structures of the MC simulation. Initially, the slab contains a nearly isotropic distribution of Cr atoms among the 15 Cr layers (layer ordering is depicted in the figure). However, the application of compressive strain in the  $x$ – $y$  plane is shown to induce an ultimate alternating distribution of Cr atoms along the  $z$ -direction. Cr atoms undergo diffusion in a manner that results in the formation of almost complete vdW gaps, with approximately 97.8% of the Cr atoms occupying the sites characteristic of a pure vdW  $\text{CrS}_2$  phase. This behavior originates from the stresses induced by compressive strain in the  $x$ – $y$  plane. As the slab is allowed to relax in the  $z$ -direction, it attempts to relieve the pressure through Poisson’s effect, leading to expansion in the  $z$ -direction, as seen in Figure 6b, where we can see that the slab experiences an expansion of 0.56 nm in the  $z$ -direction.

Figure 6d depicts the thickness evolution of the 15 layers of the  $\text{CrS}_2$  slab during the MC simulation. Initially, there is a transient period for approximately 10,000 steps during which all inner layers undergo a reduction in thickness due to the inner pressure buildup in response to the externally imposed strain (see Figure 6e), except for the surface layers (layers {1, 15}), which do not experience the same internal stresses owing to their direct exposure to vacuum. After this transient period, notable observations can be made from the data presented in Figure 6d:

- (i) All layers attempt to increase their thickness to alleviate lateral stresses. However, it is important to note that the level of resistance to this expansion varies among the layers, resulting in differing degrees of expansion for each layer. Specifically, the two surface layers (layers {1, 15}) exhibit the smallest degree of expansion. This is attributed to the net pulling force they experience

toward the center of the slab due to their exposure to vacuum, which counteracts the slab's inherent tendency to expand for pressure release. As a result, these layers maintain their attained equilibrium thickness, preserving their vertical S–Cr–S bond lengths at an equilibrium state. Thus, layers {1, 15} act as favorable sites for accommodating additional Cr atoms, resulting in the migration of vacancies away from them.

- (ii) In contrast, the neighboring inner layers {2, 14} encounter significantly smaller net pulling forces, resulting in diminished resistance to axial expansion. Consequently, layers {2, 14} undergo more substantial increase in thickness, causing the S–Cr–S bond lengths in these layers to stretch beyond the equilibrium value. As a result, these layers become higher-energy sites for Cr atoms. Accordingly, Cr atoms start to migrate from layers {2, 14} to the neighboring layers. The cumulative migration of Cr atoms from layers {2, 14} results in the formation of low-density Cr environments adjacent to layers {3, 13}, inducing a net inward pulling force on the Cr atoms in layers {3, 13}, akin to the situation observed in layers {1, 15}.
- (iii) As a consequence, layers {3, 13} exhibit higher resistance to expansion, thereby facilitating the migration of vacancies and displaying a stronger preference for accommodating Cr atoms. This phenomenon progresses toward the middle layers of the slab, leading to the formation of an alternating pattern characterized by lower-energy (Cr-rich) layers and higher-energy (Cr-deficient) layers. In Figure 6e, we can observe that the norm of  $z$ -forces acting on the even (Cr-deficient) layers exhibit higher values in comparison to the odd (Cr-rich) layers, thereby confirming the emergence of the alternating layered pattern.
- (iv) Additionally, Figure 6d reveals how the layers' expansion behavior begins to bifurcate after approximately 30,000 steps, leading to the formation of two distinct groups: one with increased thickness for the Cr-deficient layers and another with smaller thickness for the Cr-rich layers. This transition signifies the opening of vdW gaps transforming the initial strong 3D covalent bonding to weak interlayer vdW bonding between the covalently bonded CrS<sub>2</sub> layers. In other words, our findings detail the transformation of a non-vdW CrS<sub>2</sub> slab to form vdW CrS<sub>2</sub> layers.

Figure 6f illustrates the distribution of Cr atoms across the layers during the MC simulation. We can observe that the number of Cr atoms gradually decreases within the group of even (Cr-deficient/vdW gap) layers and increases within the odd (Cr-rich/CrS<sub>2</sub>) layers, where site energies are comparatively lower. More interestingly, the amplitude of diffusion rate (i.e., slope of the Cr distribution curve) exhibits a gradual increase as we approach the free surface of the slab at early stages of MC iterations. This reveals that Cr-rich/Cr-deficient alternating layer formation initially occurs at the free surfaces and propagates toward the middle layers of the slab. This point is further expounded in Figure 6g, wherein the extent of diffusivity is assessed through quantification of the number of vertical jumps made by vacancies from their initial positions. We can notice that the number of net vertical vacancy jumps is the highest for the surface layers and decreases progressively toward the central layers of the slab. Notably, the even layers

demonstrate a greater frequency of zero vacancy vertical displacements, owing to the higher-energy sites in these Cr-deficient layers that are amenable to the occupation of vacancies rather than Cr atoms. Furthermore, a symmetrical distribution of vertical vacancy jumps is observed in both the  $+z$  and  $-z$  directions, which indicates an unbiased diffusion along the  $z$  axis, as one would naturally anticipate.

The vertical diffusion of vacancies in this process exhibits a localized nature, signifying a limited diffusion length. The histogram in Figure 6g reveals that approximately 34% of vacancies remain confined within their respective layers, while about 48% diffuse to the first nn layer, 13% move to the second nn layer, and only around 5% diffuse beyond the second nn layer. This observation indicates a reduced likelihood of long-range interlayer jumps. Moreover, since the vertical displacement of vacancies is restricted to specific atomic neighborhoods, this is expected to lead to a higher occurrence of intralayer vacancy transitions. These intralayer transitions allow vacancies to explore various sites within their respective layers, potentially facilitating rearrangements that promote interlayer diffusion. Interestingly, the cumulative counts of intralayer and interlayer transitions, as depicted in Figure 6h, show comparable probabilities at initial MC steps, eventually reaching a plateau with an average of only  $\sim 1.21$  horizontal vacancy jumps for each vertical jump, which further proves the limited diffusion length associated with intralayer transitions as well. These findings offer evidence that the prevailing diffusion process is of a short-range nature, characterized by movements occurring in the immediate proximity of vacancies and their adjacent layers. As a consequence, this localized diffusion mechanism is expected to facilitate the transition from a non-vdW configuration to a vdW layered arrangement, owing to the reduced number of barriers that need to be traversed. These findings hold significant implications for the exfoliation of clean monolayer/few-layer 2D materials from non-vdW crystals through strain engineering, thereby unlocking new prospects for device-level applications and large-scale production of 2D materials.

#### 4. DISCUSSION

In this study, we presented a systematic approach for developing a highly efficient and accurate NNP to model nonstoichiometric environments prevalent during the chemical exfoliation of non-vdW systems, using Cr<sub>(1-x)</sub>S as a case study, encompassing the entire range of vacancy concentrations in the Cr sublattice. We extensively evaluated the generalizability of the NNP model by testing its configurational and local geometrical optimization capabilities across various unseen compositions.

In the domain of on-lattice configurational optimization, where the CE method is traditionally proficient, we have shown the NNP's superiority over CE, achieving significantly lower energy errors with respect to DFT. Notably, as we move from ground-state compositions of Cr<sub>(1-x)</sub>S, concentrated around (Cr<sub>0.667</sub>S), toward higher-energy nonstoichiometric phases (especially at high vacancy concentrations), the accuracy gap between the NNP and CE models becomes more apparent in on-lattice configurational optimization. This observation highlights NNP's enhanced capacity to generalize to higher-energy basins in the PES, even without explicit training on similar configurations. In contrast, CE exhibits weaker generalization in high-energy regions unless specifically trained with a broader data set encompassing both low-energy

and high-energy configurations. A recent study supports this claim and demonstrates how training CE on a larger, diverse training set of configurations generated by MLPs can improve its performance and result in more robust thermodynamic simulations.<sup>26</sup>

Although the NNP data set contains more data points than the CE data set, we should note that the configurations (atomic arrangements of Cr, S, and vacancies) in both data sets are the same. This is because the excess data points in the NNP data set consist of merely snapshots from strain/MD or strain/relaxation trajectories of the same SQS cells that comprise the CE data set. This argues that it is not the larger data set that is responsible for the better performance but rather the higher flexibility of NNP, which provides better generalization. Indeed, the higher flexibility of the NNP does come with the trade-off of a more complex model compared to CE, with a much larger basis set size, as outlined in Tables S2 and S3. This necessitates the NNP to acquire a substantially larger data set to train this expanded basis set. However, we note that around 80% of the data set provided for NNP was sampled from the nondeployed DFT relaxation calculations performed already to train CE. This suggests that instead of conventionally having CE as a final model for a non-stoichiometric system, it can be regarded as a first-step data set-sampling model for the more accurate NNP model that will be trained mostly on the idle DFT data set generated originally to fit CE.

Furthermore, we have also shown that the robust generalization of NNP to high-energy configurations at unseen compositions persists even when extrapolating to sublattice configurations beyond the scope of the training data. Despite our data set consisting exclusively of two-sublattice configurations (inactive S sublattice and active Cr/vacancy sublattice), the NNP accurately predicts configurations where Cr, S, and vacancies are allowed to occupy any lattice site.

Moreover, we meticulously examined the NNP model's accuracy in approximating the PES around the local minima corresponding to ground-state structures at unseen compositions. The results demonstrate the NNP's ability to accurately reproduce energies under elastic lattice strains beyond the training scope as well as make precise predictions of vibrational energies and forces for snapshots from MD simulations. Our investigation revealed the NNP's generalization accuracy trends when extrapolating to ground-state structures at unseen compositions. Notably, we observe a gradual degradation in performance as we move beyond the extensively trained composition range of the NNP model, especially when considering strained and vibrationally perturbed structural snapshots of ground states at far compositions.

Additionally, we demonstrated an illustrative application of the NNP model for SA optimizations. Utilizing a multiple-cycle SA algorithm, we identified the low-energy ground-state and metastable structures that are anticipated to arise from the experimental synthesis of  $\text{Cr}_{(1-x)}\text{S}$  phases in the composition range ( $0.25 \leq x \leq 0.5$ ). Within this range, the NNP model accurately predicted the three known Cr–S ground-state phases listed in the Materials Project database:<sup>89</sup>  $\text{Cr}_{0.75}\text{S}$  (mp-964),  $\text{Cr}_{0.667}\text{S}$  (mp-555569), and  $\text{Cr}_{0.375}\text{S}$  (mp-1181961). Moreover, the SA optimizations provided valuable insights into the preferred structures of Cr–S materials in this composition range. We observed a preference for structures that feature alternating  $\text{CrS}_2$  and Cr-deficient layers, where the surplus Cr atoms beyond the ratio of  $\text{Cr}/\text{S} = 1/2$  act as

intercalants within the vdW gaps between  $\text{CrS}_2$  layers. The presence of these intercalant Cr atoms in the vdW gaps significantly contributes to the stabilization of  $\text{CrS}_2$  layers, even at relatively low percentages down to around 0.03. This becomes evident in the case of the  $\text{CrS}_2$  phase, where 50% of the Cr atoms display a preferential migration to the vdW gaps to avoid the higher formation energy associated with the vdW  $\text{CrS}_2$  phase.

The NNP was further employed to investigate the influence of lateral compressive strain on  $\text{CrS}_2$  slabs, resulting in a transition from non-vdW to vdW  $\text{CrS}_2$ . The analysis demonstrated the tendency of the slabs to release the strain-induced pressure through axial Poisson's expansion, giving rise to an alternating stress pattern within the slab layers. This alternating stress prompts the migration of Cr atoms from layers of high stress to those of low stress, leading to the formation of nearly empty vdW gaps between the  $\text{CrS}_2$  layers. This behavior bears resemblance to successful endeavors in the CVD growth of vdW  $\text{CrS}_2$  slabs, where a lattice mismatch of approximately 7% arises due to the smaller lattice constant of the used f-mica substrate.<sup>10</sup> We conjecture that the smaller lattice parameter of the substrate is the reason behind the epitaxial growth of the vdW  $\text{CrS}_2$  phase, rather than a non-vdW counterpart, wherein the anticipated compressive stresses due to lattice mismatch are released through vertical expansion of layers until stable vdW gaps are formed between the  $\text{CrS}_2$  layers.

In light of the remarkable capability of the NNP model to provide energy and force predictions nearly as accurate as DFT, even for diverse and unobserved chemical compositions, atomic configurations, lattice strains, and atomic displacements, it holds great promise for steering off-lattice large-scale simulations of nonstoichiometric and partial occupancy systems. As approximately 80% of our data set originates from previously idle structures in the CE training data set, our methodology presents a cost-effective approach for modeling nonstoichiometric and partial occupancy systems using NNPs. This approach holds practical implications in predicting phase diagrams, optimizing crystal structures, and simulating vacancy diffusion dynamics, a critical process in the synthesis of 2D materials using both top-down and bottom-up methods. The kinetics of this diffusion process are intricately molded by the immediate atomic surroundings, which can undergo substantial stoichiometric variations over both spatial and temporal dimensions during materials synthesis. As a consequence, we advocate for the integration of NNPs or analogous MLPs for future computational studies on chemical exfoliation and epitaxial CVD growth of 2D materials.

This work delved into the intricate chemical and geometrical degrees of freedom inherent in nonstoichiometric systems with consideration only for the ground magnetic state obtained through spin-polarized DFT calculations. Prior studies have pioneered the combination of structural and spin degrees of freedom, enabling a comprehensive modeling that spans diverse magnetic configurations.<sup>92,93</sup> However, these models are currently limited to individual chemical configurations. Consequently, an avenue of considerable promise emerges for forthcoming studies to adeptly integrate magnetic spin degrees of freedom with the underlying chemical and geometrical attributes of nonstoichiometric systems. Such a holistic amalgamation holds the potential to significantly enhance the precision of modeling the synthesis processes of 2D magnetic

materials, thereby expediting experimental mass production in this field.

## 5. CONCLUSIONS

In conclusion, we have introduced a versatile framework that employs NNPs for modeling the nonstoichiometric characteristics inherent in the chemical exfoliation of non-vdW materials. We have convincingly demonstrated the superior performance of the NNP compared to the conventional CE model in terms of the ability to bridge DFT accuracy to unseen crystal structures and compositions. By integrating the NNP into SA, we predicted the low-energy ground-state and metastable structures for diverse  $\text{Cr}_{(1-x)}\text{S}$  compositions. A key revelation was a structural shift at  $\text{Cr}_{0.5}\text{S}$ , with half the Cr atoms migrating to vdW gaps, underscoring the non-vdW nature of  $\text{CrS}_2$  and highlighting the role of excess Cr beyond  $\text{Cr/S} = 1/2$  in vdW gap stabilization. Furthermore, we employed the NNP in an extensive vacancy diffusion MC simulation, illustrating the influential role of lateral compressive strain in promoting vdW gap formation in 2D non-vdW  $\text{CrS}_2$  slabs. This finding suggests the potential of controlled strain engineering to enhance the efficiency of exfoliating ultrathin nanosheets from non-vdW crystals. In essence, our work establishes NNPs and analogous MLPs as invaluable tools for guiding computational simulations of the chemical exfoliation of 2D non-vdW materials, with a specific emphasis on the intrinsic disordered nonstoichiometric aspects of these processes.

## ■ ASSOCIATED CONTENT

### SI Supporting Information

The Supporting Information is available free of charge at <https://pubs.acs.org/doi/10.1021/acs.jpcc.3c06168>.

Enhancing reproducibility, NNP training data set, DFT, CE, and NNP setting files, along with Python codes for SA, MC vacancy diffusion simulations, and Jupyter notebooks for result analysis, are available on GitHub (<https://github.com/UMBC-STEAM-LAB/NNP-nonstoichiometric-chromium-sulfides>)  
HYPERLINK "https://pubs.acs.org/doi/10.1021/acs.jpcc.3c06168?goto=supporting-info" \o "https://pubs.acs.org/doi/10.1021/acs.jpcc.3c06168?goto=supporting-info" https://pubs.acs.org/doi/10.1021/acs.jpcc.3c06168 (PDF)

## ■ AUTHOR INFORMATION

### Corresponding Author

Can Ataca – Department of Physics, University of Maryland Baltimore County, Baltimore, Maryland 21250, United States; [orcid.org/0000-0003-4959-1334](https://orcid.org/0000-0003-4959-1334); Email: [ataca@umbc.edu](mailto:ataca@umbc.edu)

### Authors

Akram Ibrahim – Department of Physics, University of Maryland Baltimore County, Baltimore, Maryland 21250, United States; [orcid.org/0009-0008-7311-7062](https://orcid.org/0009-0008-7311-7062)

Daniel Wines – Material Measurement Laboratory, National Institute of Standards and Technology, Gaithersburg, Maryland 20899, United States; Department of Physics, University of Maryland Baltimore County, Baltimore, Maryland 21250, United States; [orcid.org/0000-0003-3855-3754](https://orcid.org/0000-0003-3855-3754)

Complete contact information is available at: <https://pubs.acs.org/10.1021/acs.jpcc.3c06168>

## Author Contributions

A.I. trained and validated the NNP workflow, conducted DFT calculations for sampled structures, coded and executed all SA and MC simulations, and drafted the manuscript. D.W. conducted the DFT simulations of initial SQS cells sampled by CE and revised the manuscript. C.A. guided the project, oversaw all the work, and edited the manuscript.

## Notes

The authors declare the following competing financial interest(s): Certain equipment, instruments, software, or materials are identified in this paper in order to specify the experimental procedure adequately. Such identification is not intended to imply recommendation or endorsement of any product or service by NIST, nor is it intended to imply that the materials or equipment identified are necessarily the best available for the purpose.

## ■ ACKNOWLEDGMENTS

The authors acknowledge the fund from the National Science Foundation (NSF) under grant number NSF DMR-2213398.

## ■ REFERENCES

- (1) Jin, C.; Kou, L. Two-dimensional non-van der Waals magnetic layers: functional materials for potential device applications. *J. Phys. D: Appl. Phys.* **2021**, *54*, 413001.
- (2) Balan, A. P.; Puthirath, A. B.; Roy, S.; Costin, G.; Oliveira, E. F.; Saadi, M.; Sreepal, V.; Friedrich, R.; Serles, P.; Biswas, A.; Iyengar, S. A.; Chakingal, N.; Bhattacharyya, S.; Saju, S. K.; Pardo, S. C.; Friedrich, R.; Sassi, L. M.; Filleter, T.; Krashennnikov, A.; Friedrich, R.; Galvao, D. S.; Friedrich, R.; Vajtai, R.; Ajayan, P. M. Non-van der Waals quasi-2D materials; recent advances in synthesis, emergent properties and applications. *Mater. Today* **2022**, *58*, 164–200.
- (3) Hasan, M.; Ta, H. Q.; Ullah, S.; Yang, X.; Luo, J.; Bachmatiuk, A.; Gemming, T.; Trzebicka, B.; Mahmood, A.; Zeng, M.; Fu, L.; Liu, L.; Rummeli, M. H. Crystal structure, synthesis and characterization of different chromium-based two-dimensional compounds. *Arabian J. Chem.* **2023**, *16*, 104973.
- (4) Gibertini, M.; Koperski, M.; Morpurgo, A. F.; Novoselov, K. S. Magnetic 2D materials and heterostructures. *Nat. Nanotechnol.* **2019**, *14*, 408–419.
- (5) Lado, J. L.; Fernández-Rossier, J. On the origin of magnetic anisotropy in two dimensional  $\text{CrI}_3$ . *2D Materials* **2017**, *4*, 035002.
- (6) Yang, H.; Wang, F.; Zhang, H.; Guo, L.; Hu, L.; Wang, L.; Xue, D.-J.; Xu, X. Solution synthesis of layered van der Waals (vdW) ferromagnetic  $\text{CrGeTe}_3$  nanosheets from a non-vdW  $\text{Cr}_2\text{Te}_3$  template. *J. Am. Chem. Soc.* **2020**, *142*, 4438–4444.
- (7) Song, X.; Cheng, G.; Weber, D.; Pielhofer, F.; Lei, S.; Klemenz, S.; Yeh, Y.-W.; Filsinger, K. A.; Arnold, C. B.; Yao, N.; Schoop, L. M. Soft Chemical Synthesis of  $\text{H}_x\text{CrS}_2$ : An Antiferromagnetic Material with Alternating Amorphous and Crystalline Layers. *J. Am. Chem. Soc.* **2019**, *141*, 15634–15640.
- (8) Cui, F.; Zhao, X.; Xu, J.; Tang, B.; Shang, Q.; Shi, J.; Huan, Y.; Liao, J.; Chen, Q.; Hou, Y.; Zhang, Q.; Pennycook, S. J.; Zhang, Y. Controlled Growth and Thickness-Dependent Conduction-Type Transition of 2D Ferrimagnetic  $\text{Cr}_2\text{S}_3$  Semiconductors. *Adv. Mater.* **2020**, *32*, 1905896.
- (9) Chu, J.; Zhang, Y.; Wen, Y.; Qiao, R.; Wu, C.; He, P.; Yin, L.; Cheng, R.; Wang, F.; Wang, Z.; Xiong, J.; Li, Y.; He, J. Submillimeter-Scale Growth of One-Unit-Cell-Thick Ferrimagnetic  $\text{Cr}_2\text{S}_3$  Nanosheets. *Nano Lett.* **2019**, *19*, 2154–2161.
- (10) Xiao, H.; Zhuang, W.; Loh, L.; Liang, T.; Gayen, A.; Ye, P.; Bosman, M.; Eda, G.; Wang, X.; Xu, M. Van der Waals Epitaxial

Growth of 2D Layered Room-Temperature Ferromagnetic CrS<sub>2</sub>. *Adv. Mater. Interfaces* **2022**, *9*, 2201353.

(11) Song, X.; Yuan, F.; Schoop, L. M. The properties and prospects of chemically exfoliated nanosheets for quantum materials in two dimensions. *Appl. Phys. Rev.* **2021**, *8*, 011312.

(12) Ushakov, A.; Kukusta, D.; Yaresko, A.; Khomskii, D. Magnetism of layered chromium sulfides M CrS<sub>2</sub> (M = Li, Na, K, Ag, and Au): A first-principles study. *Phys. Rev. B* **2013**, *87*, 014418.

(13) Song, X.; Schneider, S. N.; Cheng, G.; Khoury, J. F.; Jovanovic, M.; Yao, N.; Schoop, L. M. Kinetics and evolution of magnetism in soft-chemical synthesis of CrSe<sub>2</sub> from KCrSe<sub>2</sub>. *Chem. Mater.* **2021**, *33*, 8070–8078.

(14) Van Bruggen, C.; Haange, R.; Wiegers, G.; De Boer, D. CrSe<sub>2</sub>, a new layered dichalcogenide. *Physica B+C* **1980**, *99*, 166–172.

(15) Freitas, D. C.; Weht, R.; Sulpice, A.; Remenyi, G.; Strobel, P.; Gay, F.; Marcus, J.; Núñez-Regueiro, M. Ferromagnetism in layered metastable 1T-CrTe<sub>2</sub>. *J. Phys.: Condens. Matter* **2015**, *27*, 176002.

(16) Stiles, J. W.; Soltys, A. L.; Song, X.; Lapidus, S. H.; Arnold, C. B.; Schoop, L. M. Unlocking High Capacity and Fast Na<sup>+</sup> Diffusion of H<sub>x</sub>CrS<sub>2</sub> by Proton-Exchange Pretreatment. *Adv. Mater.* **2023**, *35*, 2209811.

(17) Oganov, A. R. *Modern methods of crystal structure prediction*; John Wiley & Sons, 2011.

(18) Zunger, A.; Wei, S.-H.; Ferreira, L.; Bernard, J. E. Special quasirandom structures. *Phys. Rev. Lett.* **1990**, *65*, 353–356.

(19) Jiang, C. First-principles study of ternary bcc alloys using special quasi-random structures. *Acta Mater.* **2009**, *57*, 4716–4726.

(20) Zhang, Y.; Liu, B.; Wang, J. Self-assembly of Carbon Vacancies in Sub-stoichiometric ZrC<sub>1-x</sub>. *Sci. Rep.* **2015**, *5*, 18098.

(21) Ravi, C.; Sahu, H.; Valsakumar, M.; van de Walle, A. Cluster expansion Monte Carlo study of phase stability of vanadium nitrides. *Phys. Rev. B* **2010**, *81*, 104111.

(22) Xie, J.-Z.; Jiang, H. Revealing Carbon Vacancy Distribution on  $\alpha$ -MoC<sub>1-x</sub> Surfaces by Machine-Learning Force-Field-Aided Cluster Expansion Approach. *J. Phys. Chem. C* **2023**, *127*, 13228–13237.

(23) Haselmann, U.; Suyolcu, Y. E.; Wu, P.-C.; Ivanov, Y. P.; Knez, D.; Van Aken, P. A.; Chu, Y.-H.; Zhang, Z. Negatively Charged In-Plane and Out-Of-Plane Domain Walls with Oxygen-Vacancy Agglomerations in a Ca-Doped Bismuth-Ferrite Thin Film. *ACS Appl. Electron. Mater.* **2021**, *3*, 4498–4508.

(24) Aschauer, U.; Pfenninger, R.; Selbach, S. M.; Grande, T.; Spaldin, N. A. Strain-controlled oxygen vacancy formation and ordering in CaMnO<sub>3</sub>. *Phys. Rev. B* **2013**, *88*, 054111.

(25) Komsa, H.-P.; Kurasch, S.; Lehtinen, O.; Kaiser, U.; Krasheninnikov, A. V. From point to extended defects in two-dimensional MoS<sub>2</sub>: Evolution of atomic structure under electron irradiation. *Phys. Rev. B* **2013**, *88*, 035301.

(26) Xie, J.-Z.; Zhou, X.-Y.; Luan, D.; Jiang, H. Machine Learning Force Field Aided Cluster Expansion Approach to Configurationally Disordered Materials: Critical Assessment of Training Set Selection and Size Convergence. *J. Chem. Theory Comput.* **2022**, *18*, 3795–3804.

(27) Behler, J.; Parrinello, M. Generalized neural-network representation of high-dimensional potential-energy surfaces. *Phys. Rev. Lett.* **2007**, *98*, 146401.

(28) Ko, T. W.; Finkler, J. A.; Goedecker, S.; Behler, J. A fourth-generation high-dimensional neural network potential with accurate electrostatics including non-local charge transfer. *Nat. Commun.* **2021**, *12*, 398.

(29) Smith, J. S.; Isayev, O.; Roitberg, A. E. ANI-1: an extensible neural network potential with DFT accuracy at force field computational cost. *Chem. Sci.* **2017**, *8*, 3192–3203.

(30) Zhang, L.; Han, J.; Wang, H.; Car, R.; Weinan, E. Deep potential molecular dynamics: a scalable model with the accuracy of quantum mechanics. *Phys. Rev. Lett.* **2018**, *120*, 143001.

(31) Bartók, A. P.; Payne, M. C.; Kondor, R.; Csányi, G. Gaussian approximation potentials: The accuracy of quantum mechanics, without the electrons. *Phys. Rev. Lett.* **2010**, *104*, 136403.

(32) Bartók, A. P.; Kondor, R.; Csányi, G. On representing chemical environments. *Phys. Rev. B* **2013**, *87*, 184115.

(33) Shapeev, A. V. Moment tensor potentials: A class of systematically improvable interatomic potentials. *Multiscale Model. Simul.* **2016**, *14*, 1153–1173.

(34) Thompson, A. P.; Swiler, L. P.; Trott, C. R.; Foiles, S. M.; Tucker, G. J. Spectral neighbor analysis method for automated generation of quantum-accurate interatomic potentials. *J. Comput. Phys.* **2015**, *285*, 316–330.

(35) Bochkarev, A.; Lysogorskiy, Y.; Menon, S.; Qamar, M.; Mrovec, M.; Drautz, R. Efficient parametrization of the atomic cluster expansion. *Phys. Rev. Mater.* **2022**, *6*, 013804.

(36) Lysogorskiy, Y.; Oord, C. v. d.; Bochkarev, A.; Menon, S.; Rinaldi, M.; Hammerschmidt, T.; Mrovec, M.; Thompson, A.; Csányi, G.; Ortner, C.; Drautz, R. Performant implementation of the atomic cluster expansion (PACE) and application to copper and silicon. *npj Comput. Mater.* **2021**, *7*, 97.

(37) Batzner, S.; Musaelian, A.; Sun, L.; Geiger, M.; Mailoa, J. P.; Kornbluth, M.; Molinari, N.; Smidt, T. E.; Kozinsky, B. E. E(3)-equivariant graph neural networks for data-efficient and accurate interatomic potentials. *Nat. Commun.* **2022**, *13*, 2453.

(38) Chen, C.; Ong, S. P. A universal graph deep learning interatomic potential for the periodic table. *Nat. Comput. Sci.* **2022**, *2*, 718–728.

(39) Choudhary, K.; DeCost, B.; Major, L.; Butler, K.; Thiyagalingam, J.; Tavazza, F. Unified graph neural network force-field for the periodic table: solid state applications. *Digital Discovery* **2023**, *2*, 346–355.

(40) Bartók, A. P.; Kermode, J.; Bernstein, N.; Csányi, G. Machine learning a general-purpose interatomic potential for silicon. *Phys. Rev. X* **2018**, *8*, 041048.

(41) Shaidu, Y.; Küçükbenli, E.; Lot, R.; Pellegrini, F.; Kaxiras, E.; de Gironcoli, S. A systematic approach to generating accurate neural network potentials: The case of carbon. *npj Comput. Mater.* **2021**, *7*, 52.

(42) Mangold, C.; Chen, S.; Barbalinardo, G.; Behler, J.; Pochet, P.; Termentzidis, K.; Han, Y.; Chaput, L.; Lacroix, D.; Donadio, D. Transferability of neural network potentials for varying stoichiometry: Phonons and thermal conductivity of Mn<sub>x</sub>Ge<sub>y</sub> compounds. *J. Appl. Phys.* **2020**, *127*, 244901.

(43) Mortazavi, B.; Novikov, I. S.; Podryabinkin, E. V.; Roche, S.; Rabczuk, T.; Shapeev, A. V.; Zhuang, X. Exploring phononic properties of two-dimensional materials using machine learning interatomic potentials. *Appl. Mater. Today* **2020**, *20*, 100685.

(44) Deringer, V. L.; Bernstein, N.; Bartók, A. P.; Cliffe, M. J.; Kerber, R. N.; Marbella, L. E.; Grey, C. P.; Elliott, S. R.; Csányi, G. Realistic atomistic structure of amorphous silicon from machine-learning-driven molecular dynamics. *J. Phys. Chem. Lett.* **2018**, *9*, 2879–2885.

(45) Caro, M. A.; Deringer, V. L.; Koskinen, J.; Laurila, T.; Csányi, G. Growth mechanism and origin of high s p<sup>3</sup> content in tetrahedral amorphous carbon. *Phys. Rev. Lett.* **2018**, *120*, 166101.

(46) Morawietz, T.; Singraber, A.; Dellago, C.; Behler, J. How van der Waals interactions determine the unique properties of water. *Proc. Natl. Acad. Sci. U.S.A.* **2016**, *113*, 8368–8373.

(47) Li, Q.-J.; Küçükbenli, E.; Lam, S.; Khaykovich, B.; Kaxiras, E.; Li, J. Development of robust neural-network interatomic potential for molten salt. *Cell Rep. Phys. Sci.* **2021**, *2*, 100359.

(48) Daru, J.; Forbert, H.; Behler, J.; Marx, D. Coupled cluster molecular dynamics of condensed phase systems enabled by machine learning potentials: Liquid water benchmark. *Phys. Rev. Lett.* **2022**, *129*, 226001.

(49) Artrith, N. Machine learning for the modeling of interfaces in energy storage and conversion materials. *J. Phys.: Energy* **2019**, *1*, 032002.

(50) Achar, S. K.; Schneider, J.; Stewart, D. A. Using Machine Learning Potentials to Explore Interdiffusion at Metal–Chalcogenide Interfaces. *ACS Appl. Mater. Interfaces* **2022**, *14*, 56963–56974.

- (51) Tang, Z.; Bromley, S. T.; Hammer, B. A machine learning potential for simulating infrared spectra of nanosilicate clusters. *J. Chem. Phys.* **2023**, *158*, 158.
- (52) Jäger, M. O. J.; Morooka, E. V.; Federici Canova, F.; Himanen, L.; Foster, A. S. Machine learning hydrogen adsorption on nanoclusters through structural descriptors. *npj Comput. Mater.* **2018**, *4*, 37.
- (53) Rosenbrock, C. W.; Gubaev, K.; Shapeev, A. V.; Pártay, L. B.; Bernstein, N.; Csányi, G.; Hart, G. L. Machine-learned interatomic potentials for alloys and alloy phase diagrams. *npj Comput. Mater.* **2021**, *7*, 24.
- (54) Hodapp, M.; Shapeev, A. Machine-learning potentials enable predictive and tractable high-throughput screening of random alloys. *Phys. Rev. Mater.* **2021**, *5*, 113802.
- (55) Nikoulis, G.; Byggmästar, J.; Kioseoglou, J.; Nordlund, K.; Djurabekova, F. Machine-learning interatomic potential for W–Mo alloys. *J. Phys.: Condens. Matter* **2021**, *33*, 315403.
- (56) Andolina, C. M.; Bon, M.; Passerone, D.; Saidi, W. A. Robust, multi-length-scale, machine learning potential for Ag–Au bimetallic alloys from clusters to bulk materials. *J. Phys. Chem. C* **2021**, *125*, 17438–17447.
- (57) Li, X.; Li, B.; Yang, Z.; Chen, Z.; Gao, W.; Jiang, Q. A transferable machine-learning scheme from pure metals to alloys for predicting adsorption energies. *J. Mater. Chem. A* **2022**, *10*, 872–880.
- (58) Li, X.-G.; Chen, C.; Zheng, H.; Zuo, Y.; Ong, S. P. Complex strengthening mechanisms in the NbMoTaW multi-principal element alloy. *npj Comput. Mater.* **2020**, *6*, 70.
- (59) Kostiuchenko, T.; Körmann, F.; Neugebauer, J.; Shapeev, A. Impact of lattice relaxations on phase transitions in a high-entropy alloy studied by machine-learning potentials. *npj Comput. Mater.* **2019**, *5*, 55.
- (60) Men, Y.; Wu, D.; Hu, Y.; Li, L.; Li, P.; Jia, S.; Wang, J.; Cheng, G.; Chen, S.; Luo, W. Understanding Alkaline Hydrogen Oxidation Reaction on PdNiRuIrRh High-Entropy-Alloy by Machine Learning Potential. *Angew. Chem., Int. Ed.* **2023**, *62*, No. e202217976.
- (61) Wagih, M.; Larsen, P. M.; Schuh, C. A. Learning grain boundary segregation energy spectra in polycrystals. *Nat. Commun.* **2020**, *11*, 6376.
- (62) Lee, T.; Qi, J.; Gadre, C. A.; Huyan, H.; Ko, S.-T.; Zuo, Y.; Du, C.; Li, J.; Aoki, T.; Wu, R.; Luo, J.; Ong, S. P.; Pan, X. Atomic-scale origin of the low grain-boundary resistance in perovskite solid electrolyte  $\text{Li}_0.375\text{Sr}_0.4375\text{Ta}_0.75\text{Zr}_0.25\text{O}_3$ . *Nat. Commun.* **2023**, *14*, 1940.
- (63) Yokoi, T.; Noda, Y.; Nakamura, A.; Matsunaga, K. Neural-network interatomic potential for grain boundary structures and their energetics in silicon. *Phys. Rev. Mater.* **2020**, *4*, 014605.
- (64) Nishiyama, T.; Seko, A.; Tanaka, I. Application of machine learning potentials to predict grain boundary properties in fcc elemental metals. *Phys. Rev. Mater.* **2020**, *4*, 123607.
- (65) Bartók, A. P.; De, S.; Poelking, C.; Bernstein, N.; Kermode, J. R.; Csányi, G.; Ceriotti, M. Machine learning unifies the modeling of materials and molecules. *Sci. Adv.* **2017**, *3*, No. e1701816.
- (66) Tirelli, A.; Tenti, G.; Nakano, K.; Sorella, S. High-pressure hydrogen by machine learning and quantum Monte Carlo. *Phys. Rev. B* **2022**, *106*, L041105.
- (67) Schran, C.; Brezina, K.; Marsalek, O. Committee neural network potentials control generalization errors and enable active learning. *J. Chem. Phys.* **2020**, *153*, 153.
- (68) Artrith, N.; Behler, J. High-dimensional neural network potentials for metal surfaces: A prototype study for copper. *Phys. Rev. B* **2012**, *85*, 045439.
- (69) Hohenberg, P.; Kohn, W. Inhomogeneous electron gas. *Phys. Rev.* **1964**, *136*, B864–B871.
- (70) Perdew, J. P.; Burke, K.; Ernzerhof, M. Generalized gradient approximation made simple. *Phys. Rev. Lett.* **1996**, *77*, 3865–3868.
- (71) Blöchl, P. E. Projector augmented-wave method. *Phys. Rev. B* **1994**, *50*, 17953–17979.
- (72) Kresse, G.; Furthmüller, J. Efficient iterative schemes for ab initio total-energy calculations using a plane-wave basis set. *Phys. Rev. B* **1996**, *54*, 11169–11186.
- (73) Monkhorst, H. J.; Pack, J. D. Special points for Brillouin-zone integrations. *Phys. Rev. B* **1976**, *13*, 5188–5192.
- (74) Singraber, A.; Morawietz, T.; Behler, J.; Dellago, C. Parallel multistream training of high-dimensional neural network potentials. *J. Chem. Theory Comput.* **2019**, *15*, 3075–3092.
- (75) Singraber, A.; Behler, J.; Dellago, C. Library-based LAMMPS implementation of high-dimensional neural network potentials. *J. Chem. Theory Comput.* **2019**, *15*, 1827–1840.
- (76) Thompson, A. P.; Aktulga, H. M.; Berger, R.; Bolintineanu, D. S.; Brown, W. M.; Crozier, P. S.; in't Veld, P. J.; Kohlmeyer, A.; Moore, S. G.; Nguyen, T. D.; Shan, R.; Stevens, M. J.; Tranchida, J.; Trott, C.; Plimpton, S. J. LAMMPS - a flexible simulation tool for particle-based materials modeling at the atomic, meso, and continuum scales. *Comput. Phys. Commun.* **2022**, *271*, 108171.
- (77) van de Walle, A. *ATAT-A software toolkit for modeling coupled configurational and vibrational disorder in alloy systems*.
- (78) van de Walle, A. *The Alloy-Theoretic Automated Toolkit (ATAT): A User Guide*; Brown University: Providence, RI, 2019, Technical report.
- (79) Van De Walle, A. Multicomponent multisublattice alloys, nonconfigurational entropy and other additions to the Alloy Theoretic Automated Toolkit. *Calphad* **2009**, *33*, 266–278.
- (80) Behler, J. Atom-centered symmetry functions for constructing high-dimensional neural network potentials. *J. Chem. Phys.* **2011**, *134*, 074106.
- (81) Imbalzano, G.; Anelli, A.; Giofré, D.; Klees, S.; Behler, J.; Ceriotti, M. Automatic selection of atomic fingerprints and reference configurations for machine-learning potentials. *J. Chem. Phys.* **2018**, *148*, 241730.
- (82) Gu, T.; Luo, W.; Xiang, H. Prediction of two-dimensional materials by the global optimization approach. *WIREs Comput. Mol. Sci.* **2017**, *7*, No. e1295.
- (83) Sheskin, D. J. *Handbook of parametric and nonparametric statistical procedures*; Chapman and Hall/CRC, 2003.
- (84) Zuo, Y.; Chen, C.; Li, X.; Deng, Z.; Chen, Y.; Behler, J.; Csányi, G.; Shapeev, A. V.; Thompson, A. P.; Wood, M. A.; Ong, S. P. Performance and Cost Assessment of Machine Learning Interatomic Potentials. *J. Phys. Chem. A* **2020**, *124*, 731–745.
- (85) Lejaeghere, K.; Van Speybroeck, V.; Van Oost, G.; Cottenier, S. Error estimates for solid-state density-functional theory predictions: an overview by means of the ground-state elemental crystals. *Crit. Rev. Solid State Mater. Sci.* **2014**, *39*, 1–24.
- (86) Csonka, G. I.; Perdew, J. P.; Ruzsinszky, A.; Philippen, P. H.; Lebègue, S.; Paier, J.; Vydrov, O. A.; Ángyán, J. G. Assessing the performance of recent density functionals for bulk solids. *Phys. Rev. B* **2009**, *79*, 155107.
- (87) Doll, K.; Schön, J. C.; Jansen, M. Structure prediction based on ab initio simulated annealing for boron nitride. *Phys. Rev. B* **2008**, *78*, 144110.
- (88) Pannetier, J.; Bassas-Alsina, J.; Rodriguez-Carvajal, J.; Caignaert, V. Prediction of crystal structures from crystal chemistry rules by simulated annealing. *Nature* **1990**, *346*, 343–345.
- (89) Jain, A.; Ong, S. P.; Hautier, G.; Chen, W.; Richards, W. D.; Dacek, S.; Cholia, S.; Gunter, D.; Skinner, D.; Ceder, G.; Persson, K. A. Commentary: The Materials Project: A materials genome approach to accelerating materials innovation. *APL Mater.* **2013**, *1*, 011002.
- (90) Liu, C.-L.; Tseng, Y.-T.; Huang, C.-W.; Lo, H.-Y.; Hou, A.-Y.; Wang, C.-H.; Yasuhara, A.; Wu, W.-W. Atomic Imaging and Thermally Induced Dynamic Structural Evolution of Two-Dimensional  $\text{Cr}_2\text{S}_3$ . *Nano Lett.* **2022**, *22*, 7944–7951.
- (91) Yu, Y.; Xie, L.; Pennycook, S. J.; Bosman, M.; He, J. Strain-induced van der Waals gaps in GeTe revealed by in situ nanobeam diffraction. *Sci. Adv.* **2022**, *8*, No. eadd7690.
- (92) Eckhoff, M.; Behler, J. High-dimensional neural network potentials for magnetic systems using spin-dependent atom-centered symmetry functions. *npj Comput. Mater.* **2021**, *7*, 170.

(93) Novikov, I.; Grabowski, B.; Körmann, F.; Shapeev, A. Magnetic Moment Tensor Potentials for collinear spin-polarized materials reproduce different magnetic states of bcc Fe. *npj Comput. Mater.* **2022**, *8*, 13.